

# Guesswork in the gap: the impact of uncertainty in the compact binary population on source classification

Utkarsh Mali<sup>1</sup> and Reed Essick<sup>1,2</sup>

<sup>1</sup>*Canadian Institute for Theoretical Astrophysics and Department of Physics,  
University of Toronto, 60 St. George St, Toronto, ON M5S 3H8, Canada*

<sup>2</sup>*David A. Dunlap Department of Astronomy, University of Toronto,  
60 St. George St, Toronto, ON M5S 3H8, Canada*

(Dated: November 25, 2025)

The nature of the compact objects within the supposed “lower mass gap” remains uncertain. Observations of GW190814 and GW230529 highlight the challenges gravitational waves face in distinguishing neutron stars from black holes. Interpreting these systems is especially difficult because classifications depend simultaneously on measurement noise, compact binary population models, and equation of state (EOS) constraints on the maximum neutron star mass. We analyze 66 confident events from GWTC-3 to quantify how the probability of a component being a neutron star,  $P(\text{NS})$ , varies across the population. The effects are substantial, the dominant drivers of classification are the pairing preferences of neutron stars with other compact objects, and the neutron star spin distributions. The data reveals that  $P(\text{NS})$  varies between 1% – 67% for GW230529’s primary and between 51% – 100% for GW190425’s primary. By contrast,  $P(\text{NS})$  for GW190814’s secondary varies by  $\leq 10\%$ , demonstrating robustness from its high signal-to-noise ratio and small mass ratio. Analysis using EOS information tends to affect  $P(\text{NS})$  through the inferred maximum neutron star mass rather than the maximum spin. As it stands,  $P(\text{NS})$  remains sensitive to numerous population parameters, limiting its reliability and potentially leading to ambiguous classifications of future GW events.

## I. INTRODUCTION

Gravitational wave (GW) astronomy has revolutionized our understanding of compact objects. Over the course of four observing runs, O1 [1], O2 [2, 3], O3 [4, 5], and most recently O4a [6, 7], the LIGO-Virgo-KAGRA (LVK) collaboration has detected hundreds of compact binary mergers [8–10]. While binary black hole (BBH) mergers dominate the catalog, several binary neutron star (BNS) and neutron star–black hole (NSBH) systems have also been identified. The landmark detection of GW170817 during O2 provided the first confirmed BNS merger and catalyzed the era of multi-messenger astronomy [11]. Subsequent observing runs have added to the diversity of detected systems, including candidate BNS and NSBH mergers GW190425 [12], GW190814 [13–15], GW200105 and GW200115 in O3 [16] and GW230529 in O4 [17]. Notably GW190814 and GW230529 include compact objects with an inferred mass consistent with the putative *lower mass gap*. Here we use “lower mass gap” to denote the mass range, commonly interpreted as the region between the maximum neutron star (NS) mass [18–35] and the minimum black hole (BH) mass [36–45]. Its existence and precise bounds remain under active debate [46, 47]. As a result, mergers in this range serve as key probes of the NS to BH transition, a region where compact object formation is still uncertain.

The idea of a lower mass gap predates gravitational wave observations and was first motivated by the absence of  $3 - 5M_{\odot}$  black holes in X-ray binaries [48–50]. A plausible explanation for the gap could be due to core-collapse supernovae, in which, following the formation of the proto-NS, the efficiency of neutrino heating

plays a key role in fallback accretion. Sufficient neutrino heating drives a successful explosion that ejects most of the overlying material, yielding a stable NS (i.e., rapid timescale accretion  $\sim 10\text{ms}$ ). In contrast, insufficient heating leads to shock stagnation and substantial fallback (i.e., delayed timescale accretion  $\sim 200\text{ms}$ ), driving the remnant beyond the stability threshold and producing a BH that is typically several solar masses more massive [48, 51–56]. Both GW and electromagnetic detections have begun to challenge the existence of a sharp gap [49, 50, 57–65], with events such as GW190425, GW190814 and GW230529 consistent with component masses extending into the gap. These detections suggest that the lower mass gap may not be completely empty, but rather sparsely populated. Yet the interpretation of these events remains uncertain. For example, the classification of GW230529’s primary may depend on the assumed spin and mass priors [66] or the inclusion of tidal measurements in the GW waveform (recovery template). These systematics are explored in Cotturone et al. [67].

The NS equation of state (EOS) sets the theoretical maximum mass for a stable NS [68–77]. Rapid rotation can increase the support for heavy NS by 30% [78, 79]. Collectively, these EOS-dependent effects introduce uncertainty in the maximum mass a NS can support.

In this work, we investigate how assumptions about the underlying population of compact binaries influence the classification of low mass events. For events like GW190425 or GW230529, where the component masses are consistent with both NSs and BHs, the inferred classification can shift significantly depending on the assumed population model. By explicitly studying the population-level distributions over masses and spins, we assess how these assumptions propagate into event-level classifica-

tion.

Explicitly, a population model that enforces a sharp mass gap or favors anti-aligned spin between the two compact objects can suppress support for higher-mass events, even when the data alone remains ambiguous. We systematically explore how variations in population assumptions affect the classification of compact objects as either NS or BH. We henceforth refer to this as  $P(\text{NS})$ , with  $P(m < \gamma_{\text{low}})$  representing the population-only analysis and  $P(m < m_{\text{max}}^{\text{EOS}})$  denoting the EOS-informed analyses. Here,  $\gamma_{\text{low}}$  and  $m_{\text{max}}^{\text{EOS}}$  correspond to the boundaries taken to represent the NS-BH transition in their respective cases, with the former motivated by features in the inferred mass distribution and the latter by the maximum mass supported by the NS EOS.

The remainder of this paper is structured as follows. In Section II, we describe our methodology for hierarchical Bayesian inference, including a flexible parametric population model (FULLPOP-4.0 and extensions) [40, 61, 80, 81]. We then outline the calculation of  $P(\text{NS})$  based on Essick and Landry [82], including extensions to account for maximally spinning NS. In Section III, we present our main population fits and  $P(\text{NS})$  results, including a comprehensive “classification matrix” (Table I) that maps how population parameters affect classification. We also highlight our main results in Table II. This matrix forms the conceptual backbone of the paper, motivating a series of focused investigations into specific event-level degeneracies.

Sections IV and V explore the dominant event-level degeneracies  $q - m_1$ ,  $q - m_2$ , and  $q - \chi_{\text{eff}}$ . These sections investigate classification outcomes, particularly for low SNR events like GW230529 where degeneracies are more pronounced. We show that in high SNR events like GW190814, some of these degeneracies begin to break. In Section VI, we examine potential extensions of this work. Additional methodological details, including the definition of our population model and further discussions about GW230529, are provided in the Appendices.

## II. METHODOLOGY

### A. Hierarchical Bayesian Inference

We construct a hierarchical population model and use 66 confidently detected compact-binary coalescences (CBCs) assigned a False-Alarm-Rate (FAR) of less than 0.25 per year by at least one search within the LVK’s third gravitational wave catalog (GWTC-3) to simultaneously infer the joint mass, redshift, and spin astrophysical distributions. We assume CBCs follow an inhomogeneous Poisson process and marginalize over the overall rate of mergers. Given parameters that describe the CBC merger density and other population parameters ( $\Lambda$ ), the

likelihood of observed data ( $d_i$ ) for each event ( $i$ ) is then

$$p(\{d_i\}|\Lambda) \propto \frac{1}{\mathcal{E}^N} \prod_{i=1}^N \mathcal{Z}_i \quad (1)$$

where we have defined the single-event evidence  $\mathcal{Z}_i$

$$\mathcal{Z}_i(\Lambda) = p(d_i|\Lambda) = \int p(d_i|\theta)p(\theta|\Lambda)d\theta \quad (2)$$

and the probability of detection  $\mathcal{E}$

$$\mathcal{E}(\Lambda) = P(\mathbb{D}|\Lambda) = \int P(\mathbb{D}|\theta)p(\theta|\Lambda)d\theta \quad (3)$$

Within these integrals,  $\theta$  represents the single-event parameters, like component masses, redshift and spins,  $p(d_i|\theta)$  is the likelihood of obtaining  $d_i$  given a signal described by  $\theta$ , and  $P(\mathbb{D}|\theta)$  is the probability that a signal described by  $\theta$  would be detected marginalized over noise realizations [83–85]. See Refs. [86–90] for reviews.

Our set of 66 confident events from GWTC-3 were obtained by selecting events for which at least one search (either cWB [91], GstLAL [92], MBTA [93], and one of two PyCBC searches [94]) reported a false alarm rate (FAR)  $\leq 0.25/\text{year}$ . Since the updated GWTC-4.0 catalog contains no new BNS, we have not included the new events in our population fit. However, we include GW230529 in our classification tests. A longer explanation can be found in Appendix B. We use the joint O1+O2+O3 sensitivity estimates, where O1 and O2 estimates are semi-analytic and O3 estimates include real search sensitivity [95].

Additionally, we consider events across the entire mass spectrum, including BNS, NSBH, and BBH coalescences. Some other analyses have focused on either just the BNS or NSBH mergers, typically applying mass cuts while not always accounting for the corresponding changes in the detection probability  $P(\mathbb{D}|\Lambda)$ . We instead treat selection effects consistently [95]. We find that the BBH portion of the mass and spin distributions weakly links to BNS and NSBH events and therefore has minimal effect on classification. We nevertheless use the entire CBC population to capture the full behavior within the lower mass gap.

We adopt the FULLPOP-4.0 population model outlined in Equation A2 and Figure 11 to describe the mass, spin, and redshift distributions of compact binaries. This model builds upon the framework first introduced by Fishbach et al. [40], with subsequent extensions presented in Farah et al. [61], Mali and Essick [80] and finalized in GWTC-4.0 [81]. Given that our analysis is based on GWTC-3, we do not explicitly model an upper mass gap because the catalog contains too few high-mass events to meaningfully constrain such a feature [96].

For the redshift distribution (Equation A12), we assume mergers are uniformly distributed in comoving volume and source-frame time, with a redshift-dependent merger rate that scales as  $(1+z)^k$ .

The spin magnitude distribution (shown in Equation A10 and Figure 3) for  $\chi_1, \chi_2$  is modeled using separate truncated Gaussians, distinguishing between binaries that may contain at least one NS and those composed purely of BHs (i.e., the spin magnitude depends on the component mass with a switch point  $m_{\text{break,spin}} = 3M_\odot$ ). Similarly, the spin tilt described by  $\cos \theta_1, \cos \theta_2$  is outlined by Equation A11. It uses a mixture model combining a uniform distribution with a truncated Gaussian. As with the spin magnitudes, we adopt distinct tilt distributions for NS containing systems and for BH-only binaries to reflect differences in their likely formation channels [97] (i.e., mass dependent distribution for  $\cos \theta_i$  with a switch point  $m_{\text{break,spin}} = 3M_\odot$ ).

The entire set of population hyperparameters along with the respective priors are described in Appendix A.

## B. Classifying Compact Objects

Essick and Landry [82] introduce a mass based framework for estimating whether a compact object is consistent with a NS along with its uncertainty. This was generalized to a joint mass–spin framework within the LVK’s analysis of GW230529 [17]. The method is implemented in the open-source `mmax-model-selection` package [98], which builds upon `gw-distributions` [99]. This analysis assumes that all objects that have masses and spins consistent with a NS are NSs, which consequently results in upper limits on  $P(\text{NS})$ .

We begin by defining a region in the mass-spin parameter space where NSs exist.

$$\Theta_{\text{NS}}(m) = \Theta(m \leq \gamma_{\text{low}}) \quad (4)$$

Here,  $\Theta$  is the Heaviside step function,  $m$  is the object’s mass and  $\gamma_{\text{low}}$  is a mass scale in the population that determines the start of the lower mass gap [61]. Alternatively we can compare against mass and spin limits set by the EOS.

$$\begin{aligned} \Theta_{\text{NS}}(m, \chi) &= \Theta(m \leq m_{\text{max}}(\text{EOS}, \chi)) \\ &\times \Theta(\chi \leq \chi_{\text{max}}(\text{EOS})) \end{aligned} \quad (5)$$

Above,  $m_{\text{max}}$  and  $\chi_{\text{max}}$  denote the EOS-dependent upper limits on NS mass and spin. To model these limits, we adopt empirical relations for the maximum mass of rotating NS taken from Breu and Rezzolla [79].

$$\chi_{\text{max}} = 0.5543 C_{\text{TOV}}^{-1/2} \quad (6)$$

$$\frac{m_{\text{max}}}{m_{\text{TOV}}} = 1 + 0.4283 C_{\text{TOV}} \chi^2 + 0.7533 C_{\text{TOV}}^2 \chi^4 \quad (7)$$

where  $C_{\text{TOV}} = Gm_{\text{TOV}}/(c^2 r_{\text{TOV}})$  is the compactness of a non-rotating NS at the Tolman-Oppenheimer-Volkoff (TOV) mass limit;  $m_{\text{TOV}}$  and  $r_{\text{TOV}}$  are the corresponding mass and radius at that limit.

To estimate the probability that an object falls within this allowed region, we consider a joint posterior distribution over the population hyperparameters  $\Lambda$ , the EOS, and the event-level parameters  $\theta$  (which include  $m$  and  $\chi$ ) given some gravitational wave catalog  $H$  which includes the data for individual events [100]. The probability that the object is consistent with a NS is then:

$$\begin{aligned} P(\text{NS}) &= \int d\Lambda d\text{EOS} d\theta p(\Lambda, \text{EOS}, \theta | H) \Theta_{\text{NS}}(\theta) \\ &= \int d\Lambda d\text{EOS} p(\Lambda, \text{EOS} | H) \int d\theta p(\theta | \Lambda, H) \Theta_{\text{NS}}(\theta) \end{aligned} \quad (8)$$

This decomposition separates the joint distribution into a population-level component and an event-level component, which is often convenient for handling separate population and event-level samples. For each event of interest  $i$ , the event-level posterior is simply the single-event posterior conditioned on its data  $d_i$ :  $p(\theta | \Lambda, H) = p(\theta | \Lambda, d_i)$ . See Appendix D for more details.

Examples of  $P(\text{NS})$  can be found in Figure 1, which shows how  $P(\text{NS})$  varies across different realizations of the pairing preferences of NSs with other compact objects, encoded by the hyperparameter  $\beta_{\text{LL}}$ . Here, “pairing” refers to a NS’s preference to be partnered with another compact objects of a similar mass. Larger  $\beta_{\text{LL}}$  favors equal-mass BNS pairings, whereas smaller values favor unequal-mass systems. Current data place only weak constraints on  $\beta_{\text{LL}}$ , so very different pairing behaviors have similar posterior probability. Nonetheless these hyperparameter values can drive large swings in  $P(\text{NS})$ .

## III. MAIN RESULTS

In this section, we proceed in three steps. First, we summarize the population model. Next, we map how key hyperparameters influence  $P(\text{NS})$ , with the key features highlighted in Table I. We then quantify the resulting shifts in  $P(\text{NS})$  for each hyperparameter across events, reported in Table II. Finally, we compare population-only and EOS-informed analyses to highlight conclusions that are robust. We do not consider GW170817 in detail, as its high SNR and relatively low component masses make its classification as a BNS essentially certain across models.

### A. Inferred population model

We use FULLPOP4.0 population model, with an additional NS peak, a modified spin prescription, and the standard redshift-evolution model (see Appendix A for details). Figure 2 shows the inferred latent mass distribution across the entire mass spectrum [81]. The curve rises steeply at  $1-2M_\odot$ , then dips sharply between  $3-5M_\odot$  before recovering the familiar BBH regime. The inclusion

TABLE I. Summary of how key population features affect the probability that a component is a NS,  $P(\text{NS})$ , under two modeling choices: population-only  $P(m < \gamma_{\text{low}})$  and EOS-informed  $P(m < m_{\text{max}}^{\text{EOS}})$ . Ticks ( $\checkmark$ — $\checkmark\checkmark\checkmark$ ) denote the effect of a hyperparameter on classification with  $\checkmark$  being a weak correlation and  $\checkmark\checkmark\checkmark$  being a very strong correlation:  $\times$  denotes negligible relation to  $P(\text{NS})$ . Each feature is tied to specific hyperparameters in the population model: the lower and upper edges of the NS–BH dip are controlled by  $\gamma_{\text{low}}$  and  $\gamma_{\text{high}}$ ; the equal mass preference (“pairing”) by  $\beta_{\text{LL}}$ ; the spin magnitude distribution by  $\mu_{\chi}^{\text{low}}$  (mean) and  $\sigma_{\chi}^{\text{low}}$  (width); the spin tilt distribution by  $\mu_{\cos\theta}^{\text{low}}$  and  $\sigma_{\cos\theta}^{\text{low}}$ ; and the NS mass peak with  $\mu_{\text{peak}}^{\text{NS}}$  (location) and  $\sigma_{\text{peak}}^{\text{NS}}$  (width).  $\beta_{\text{LL}}$  and  $\mu_{\cos\theta}^{\text{low}}$  strongly affect  $P(\text{NS})$ . The strong correlation with  $\gamma_{\text{low}}$  in the population-only analysis is expected as this directly compares objects masses to  $\gamma_{\text{low}}$  (see Sec. IV A).

Param	Physical Feature	Refs	Low SNR		Asymmetric Masses	
			Population	EOS	Population	EOS
$\gamma_{\text{low}}$	Lower edge of the NS–BH Dip	(Sec IV A)	$\checkmark\checkmark\checkmark$	$\times$	$\checkmark\checkmark\checkmark$	$\times$
$\gamma_{\text{high}}$	Upper edge of the NS–BH Dip	(Sec IV B)	$\times$	$\times$	$\times$	$\times$
$\beta_{\text{LL}}$	Pairing between BNS	(Sec IV C)	$\checkmark\checkmark\checkmark$	$\checkmark\checkmark\checkmark$	$\checkmark$	$\checkmark$
$\mu_{\chi}^{\text{low}}, \sigma_{\chi}^{\text{low}}$	Spin Magnitude distribution of NS	(Sec V B)	$\checkmark\checkmark$	$\checkmark\checkmark$	$\times$	$\times$
$\mu_{\cos\theta}^{\text{low}}, \sigma_{\cos\theta}^{\text{low}}$	Spin Tilt distribution of NS	(Sec V A)	$\checkmark\checkmark\checkmark$	$\checkmark\checkmark$	$\checkmark$	$\checkmark$
$\mu_{\text{peak}}^{\text{NS}}, \sigma_{\text{peak}}^{\text{NS}}$	Peak in the NS mass distribution	(Sec IV D)	$\checkmark\checkmark$	$\checkmark$	$\times$	$\times$

of an explicit NS-peak does not greatly alter the overall shape of the mass distribution and remains consistent with expectation from existing population studies [80, 81].

Figure 3 presents the inferred spin distributions split into two mass regimes to capture potentially distinct physics above and below  $3 M_{\odot}$ . The upper panel shows the spin magnitude distribution,  $p(\chi | \text{GWTC-3})$ , while the lower panel shows the tilt distribution,  $p(\cos\theta | \text{GWTC-3})$ . For objects below  $3 M_{\odot}$  (red), the spin magnitude distribution is confined to  $\chi \leq 0.4$ , a limit set by the O3 injection coverage [85]. Within this range, the distribution peaks at low spin values, consistent with expectations for NSs. For higher-mass objects (yellow), the distribution has a longer tail extending to moderate spins, indicative of the broader spin support in the BH population. In the tilt distribution (bottom panel), both mass regimes show broadly overlapping uncertainty bands and a mild preference for aligned spins. This mass-dependent break in the spin distributions allows the analysis to isolate spin-dependent physics for low mass objects.

We do not show our redshift model as it is identical to many other population analysis [81, 86, 95]. Refer to Appendix A for a detailed outline of all models.

## B. Inferred neutron star probabilities $P(\text{NS})$

We now move from population-level structure to event-level consequences. For each event,  $P(\text{NS})$  is evaluated by marginalizing over hyperposterior samples from our population fit (population-only:  $P(m < \gamma_{\text{low}})$ ; EOS-informed:  $P(m < m_{\text{max}}^{\text{EOS}})$ ). To compute our results (sum-

marized in Table II), we artificially fix a single hyperparameter at a trial value while drawing the remaining hyperparameters from their hyperposterior. This isolates the response of  $P(\text{NS})$  to that specific feature (e.g., pairing preferences, spin magnitudes/tilts etc). We then iterate this over the prior range of the trial hyperparameter to generate an illustrative plot. Although this procedure does not reflect the fully self-consistent joint hyperposterior (because one parameter is held fixed without conditioning the posterior distribution over the rest of the hyperparameters), it is informative about the magnitude and direction of the changes to  $P(\text{NS})$ . We repeat this method across the range of hyperparameters outlined in Table II.

Uncertainties on  $P(\text{NS})$  arise from the finite Monte Carlo variance from a limited number of hyperposterior draws and event-level posterior samples.

Across the two classification schemes, we find that changes in the population model have broadly comparable impacts on  $P(\text{NS})$  for population-only ( $P(m < \gamma_{\text{low}})$ ) and EOS-informed ( $P(m < m_{\text{max}}^{\text{EOS}})$ ) analyses. We next examine joint structure in the  $q-m_1$ ,  $q-m_2$ , and  $q-\chi_{\text{eff}}$  planes.

## IV. THE $q \leftrightarrow m_1, m_2$ PLANE

We organize this section around correlations in two planes:  $q-m_1$  and  $q-m_2$ . This correlation arises because, for a fixed chirp mass  $\mathcal{M}_c$  (which is tightly constrained by the waveform phase evolution), changes in  $q$  require compensating shifts in  $m_1$  and  $m_2$  to preserve  $\mathcal{M}_c$ . Figure 4 shows the  $q-m_1$  and  $q-m_2$  correlations using the default prior distributions used to estimate the source

TABLE II. Summary of classification outcomes for key hyperparameters across GW190425’s primary, GW190814’s secondary and GW230529’s primary. We compare both the population-only (Equation 4) and EOS-informed (Equation 5) analyses. We show the range of  $P(\text{NS})$  spanned when varying each parameter, with the bottom row reporting the overall maximum change. In order to compute the largest change, we used the most extreme settings (see Section V C).

<b>Param Varied</b>	<b>GW190425 primary</b>		<b>GW190814 secondary</b>		<b>GW230529 primary</b>	
	<b>Population</b>	<b>EOS</b>	<b>Population</b>	<b>EOS</b>	<b>Population</b>	<b>EOS</b>
$\sigma_{\text{peak}}^{\text{NS}}$	93% – 99%	67% – 96%	72% – 73%	7% – 9%	18% – 37%	2% – 6%
$\beta_{\text{LL}}$	90% – 99%	60% – 98%	73% – 73%	7% – 10%	6% – 53%	0% – 18%
$\mu_{\cos\theta}^{\text{low}}$	95% – 99%	80% – 97%	68% – 75%	3% – 12%	5% – 48%	0% – 9%
$\mu_{\text{peak}}^{\text{NS}}$	96% – 97%	84% – 90%	72% – 73%	7% – 9%	26% – 46%	3% – 9%
$\gamma_{\text{high}}$	97% – 97%	87% – 90%	73% – 73%	7% – 9%	31% – 32%	4% – 5%
$\sigma_{\chi}^{\text{low}}$	97% – 100%	87% – 100%	74% – 74%	6% – 10%	18% – 35%	0% – 7%
$\mu_{\chi}^{\text{low}}$	97% – 99%	87% – 97%	72% – 73%	6% – 12%	18% – 57%	0% – 20%
$\mu_{\cos\theta}^{\text{low}} \& \beta_{\text{LL}}$	88% – 100%	51% – 100%	68% – 75%	4% – 13%	1% – 67%	0% – 21%

parameters of GW170817, GW190425 and GW230529 [7, 11, 81]. We refer back to these corner plots throughout our discussion. Motion toward more symmetric mass ratios ( $q \rightarrow 1$ ) always drives  $m_1$  downward and  $m_2$  upward. These directions do not depend on SNR. However, at low SNR, broad single-event posteriors allow stronger influence from priors, whereas at high SNR the single event posteriors are much narrower, limiting the effect of the  $q \leftrightarrow m_1, m_2$  correlations. Below, we describe how specific hyperparameters impact  $P(\text{NS})$ .

#### A. The $\gamma_{\text{low}}$ population case is prior dominated

Varying the lower edge of the NS-BH dip, and then counting the number of reweighted samples below it produces a 0–100% lever on classification. By construction, any increase (decrease) in  $\gamma_{\text{low}}$  includes (excludes) a portion of the reweighted single-event posterior. As a result, this effect does not reveal a genuine correlation in the  $q - m_1, m_2$  degeneracy. For this reason, although  $\gamma_{\text{low}}$  can strongly change  $P(m < \gamma_{\text{low}})$ , we do not interpret it as a physical effect for our analysis, and we do not emphasize it further.

In the EOS-informed analyses, variations in  $\gamma_{\text{low}}$  show no discernible correlation with  $P(m < m_{\text{max}}^{\text{EOS}})$ , although the nominal values differ from the population-only results. This is expected, as the EOS-informed classification employs a different boundary for the NS-BH transition. Overall,  $P(m < m_{\text{max}}^{\text{EOS}})$  varies by at most 4% across events (GW230529: 4% – 7%, GW190425: 87% – 91% and GW190814: 6 – 10%, among others). This limited change may seem counterintuitive, given that the location of the NS-BH boundary should, in principle, influence classification. However,  $\gamma_{\text{low}}$  does not strongly alter the inferred shape of the mass distribution. The inferred “notch amplitude” is small ( $A \sim 0.1$ ), so the model doesn’t carve a deep low mass gap. Instead the mass dis-

tribution is dominated by the peaks (see Appendix A for a definition of the notch amplitude). By contrast, Farah et al. [61] infer a larger notch amplitude, yielding a deeper gap in the mass distribution. However, their model did not include peaks and adopts a fixed mass-independent spin distribution with a redshift distribution that did not evolve with the star formation rate. A version of this model was used in the GW230529 discovery paper [17]. Further discussion about the gap depth can be found in Section 4.3 of the LVK GWTC-4.0 populations paper [81]. As a result of this, the EOS-informed classification is insensitive to variations in  $\gamma_{\text{low}}$ .

#### B. The upper edge of the NS-BH gap minimally affects $P(\text{NS})$

Across all events considered, varying  $\gamma_{\text{high}}$  produces no significant change in  $P(\text{NS})$ . Consequently, we do not include a dedicated  $\gamma_{\text{high}}$  figure. Furthermore, since the inferred notch amplitude is small, shifting  $\gamma_{\text{high}}$  minimally changes the mass distribution.

In principle, increasing the upper edge (larger  $\gamma_{\text{high}}$ ) could push support to higher  $m_1$  and thereby pull  $m_2$  lower, which might alter  $P(\text{NS})$ . In practice, however, our catalog lacks the specific event needed for this to occur. Without this “ $m_1$  near  $\gamma_{\text{high}}$  to  $m_2$  near  $\gamma_{\text{low}}$ ” configuration, the indirect pathway for  $\gamma_{\text{high}}$  to modify  $P(\text{NS})$  is limited.

#### C. Pairing (preferring equal mass binaries) pushes reweighted posteriors up the $q - m_1$ plane.

The preference which low-mass objects have in merging with companions of equal mass significantly increases  $P(\text{NS})$  under both population-only and EOS-informed analyses. The pairing hyperparameter  $\beta_{\text{LL}}$  acts

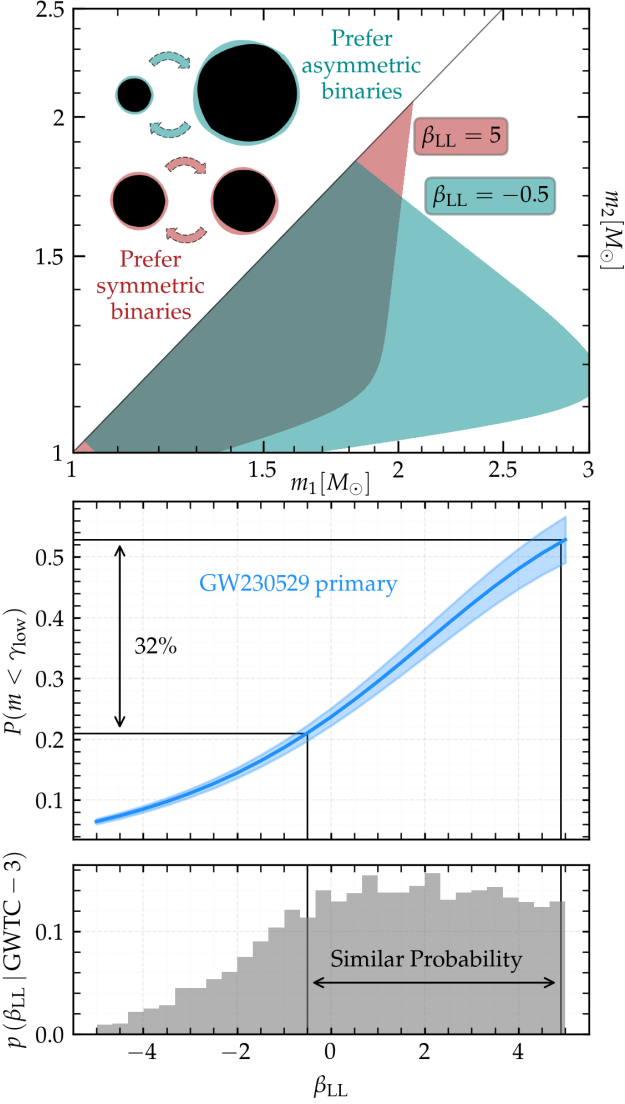


FIG. 1. The pairing of low mass compact objects ( $\beta_{LL}$ ) effect on classification of GW230529’s primary. Here, “pairing” refers to the low-mass population hyperparameter  $\beta_{LL}$  that governs how strongly binaries prefer near-equal component masses. **(Top)** Joint BNS mass distribution  $p(m_1, m_2 | \beta_{LL}, \text{GWTC-3})$  evaluated across pairing functions with comparable posterior support. Strong pairing ( $\beta_{LL} = 5$ ) favors near equal masses, while weak pairing ( $\beta_{LL} = -0.5$ ) skews toward more asymmetric binaries. **(Middle)** The probability of classifying GW230529’s primary as a NS for various  $\beta_{LL}$ ;  $\gamma_{\text{low}}$  represents the start of the NS–BH boundary. The shaded region represents the 90% symmetric credible interval around the mean.  $P(\text{NS})$  varies by up to 32% for equally likely  $\beta_{LL}$  and between 6% – 53% in total. **(Bottom)** Hyperposterior  $p(\beta_{LL} | \text{GWTC-3})$ . A wide range of  $\beta_{LL}$  values have comparable probabilities.  $\beta_{LL}$  spans values that meaningfully affect the mass distribution; for larger  $\beta_{LL}$ , the inferred  $p(m_1, m_2 | \beta_{LL}, \text{GWTC-3})$  changes very little.

directly on  $q$  through the pairing function shown in Equation A3 and Figure 4. Increasing  $\beta_{LL}$  redistributes pos-

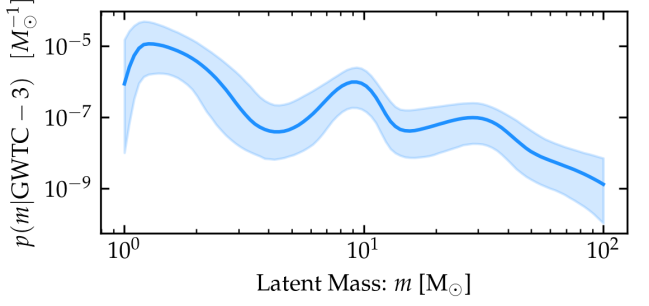


FIG. 2. Inferred latent mass distribution  $p(m)$  from GWTC-3.0. The solid curve shows the mean, while the shaded band denotes the 90% symmetric credible interval. A clear dip appears across the putative NS–BH gap, with BBH peaks near  $m \sim 10 M_\odot$  and  $m \sim 30 M_\odot$ .

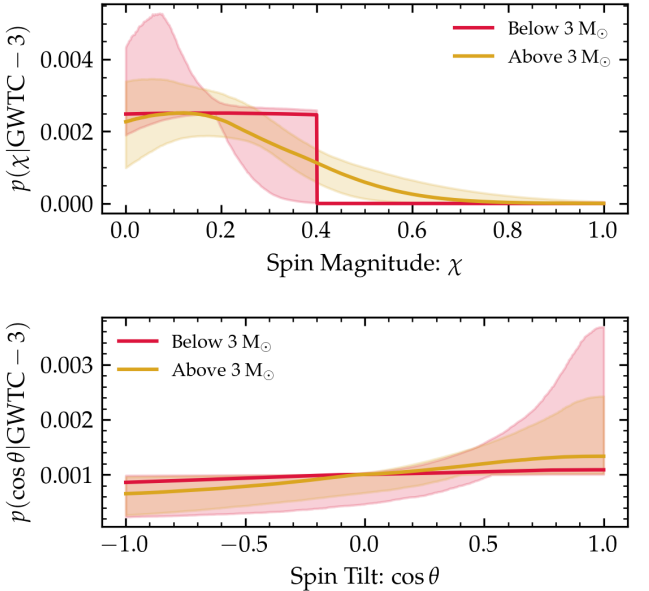


FIG. 3. Population spin distributions inferred from GWTC-3. **(Top)** Spin magnitude distributions for components below and above  $3 M_\odot$ . **(Bottom)** Corresponding spin tilt ( $\cos \theta$ ) distributions. The solid curve shows the mean, while the shaded band denotes the 90% symmetric credible interval.

terior weight toward  $q \sim 1$ . In the  $q - m_1$  plane, this slides the probability down to lower  $m_1$ , and, in the  $q - m_2$  plane, it pulls support toward larger  $m_2$ . When the secondary is confidently in the NS range (typical for many ambiguous BNS and NSBH), the preference for equal-mass mergers drags the primary below the NS boundary, increasing  $P(\text{NS})$  for the primary. For GW230529, explicitly varying the pairing function can vary  $P(\text{NS})$  by up to 46%. Similar behavior can be observed in the EOS-informed GW190425 results that span 60% to 98%. This behavior is evident in Figures 1 and 5, where larger  $\beta_{LL}$  compresses the credible region to  $q \sim 1$ .

While stronger pairing generally increases  $P(\text{NS})$  for

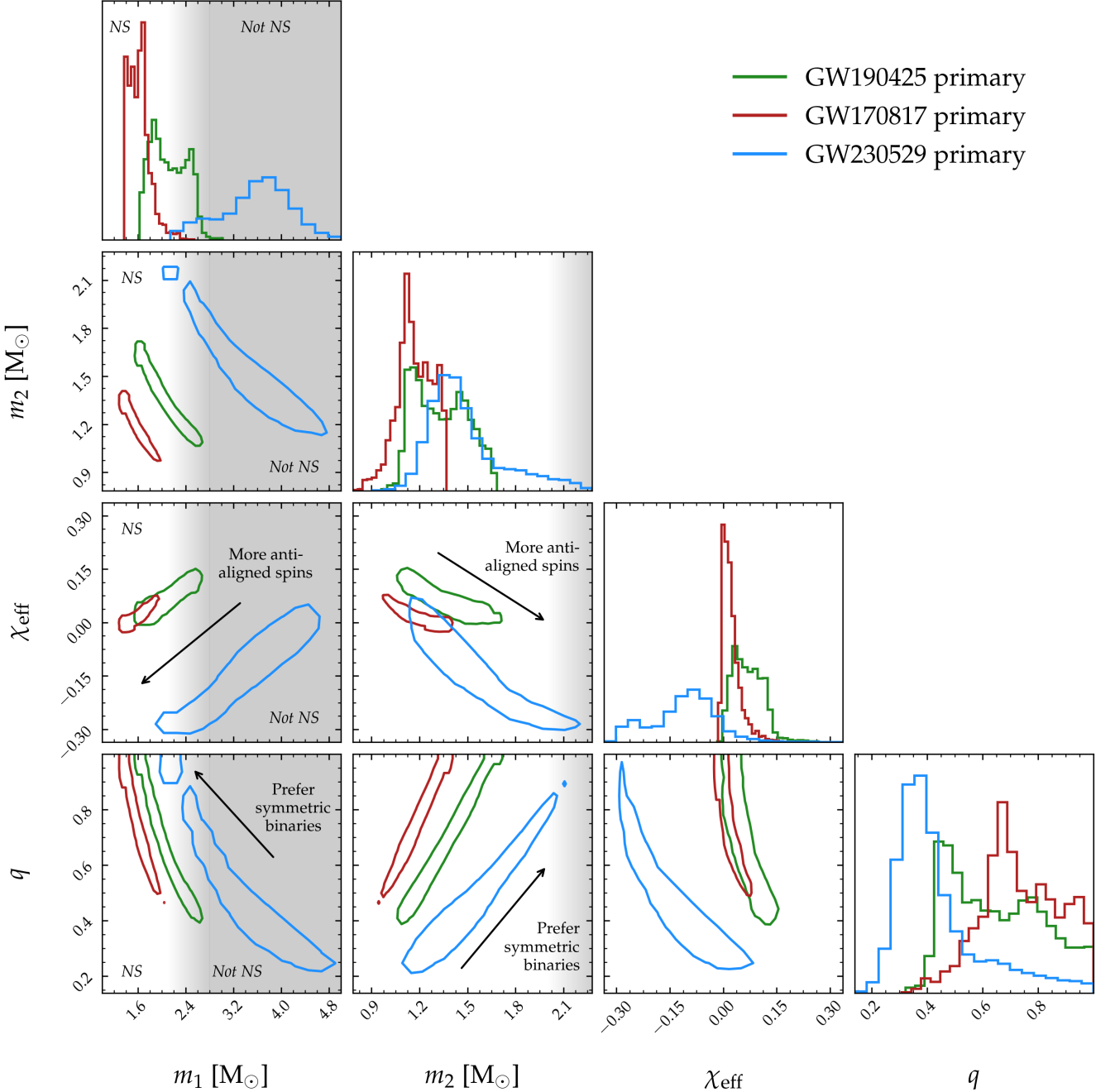


FIG. 4. Using default priors (uniform component masses in the detector frame and spins that are uniform in magnitude and isotropic in orientation), we show the inferred parameters for three events, GW170817 (red), GW190425 (green), and GW230529 (blue). Off-diagonal panels show 90% symmetric credible intervals. Gray shading indicates regions that are incompatible with NSs (masses above the NS cutoff,  $\gamma_{\text{low}}$ , or  $m_{\text{max}}^{\text{EOS}}$  in our case) and the associated uncertainty band. Degeneracies appear between  $q$ ,  $\chi_{\text{eff}}$ ,  $m_1$ , and  $m_2$ . Overall, the  $q - \chi_{\text{eff}}$ ,  $q - m_1$ , and  $q - m_2$  couplings control whether the probability crosses into the “NS” or “Not NS” demarcations.

BNS primaries, the same shift often decreases  $P(\text{NS})$  for NSBH secondaries. This is a geometric consequence of moving along the  $m_1 - m_2$  plane. Conversely, for high SNR asymmetric systems (e.g. GW190814), the likelihood anchors the single-event posterior around low  $q$ .

Thus, the same increase in pairing will not shift the reweighted  $m_2$  posterior. As a result, for GW190814, there is little to no change in  $P(\text{NS})$ . In short,  $\beta_{\text{LL}}$  has the largest effect on  $P(\text{NS})$  when the detected event is low SNR. It also impacts  $m_1$  and  $m_2$  in opposite directions.

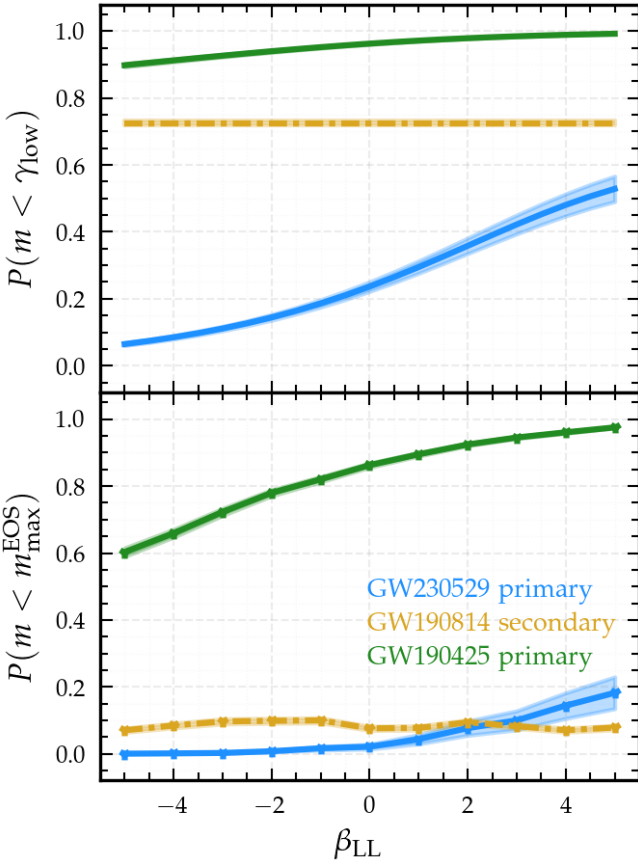


FIG. 5. The BNS pairing function’s ( $\beta_{\text{LL}}$ ) effect on classification  $P(\text{NS})$ . **(Top)** Population-only,  $P(m < \gamma_{\text{low}})$ . **(Bottom)** EOS-informed,  $P(m < m_{\text{max}}^{\text{EOS}})$ . Increasing  $\beta_{\text{LL}}$  strengthens equal mass pairing ( $q \rightarrow 1$ ). This is most apparent in GW230529’s primary (top blue, shifting by 46%) and GW190425  $m_1$  EOS case (bottom green, shifting by 37%). The shaded region represents 90% credible interval around the mean. Primaries are solid lines and secondaries are dotted lines.

#### D. A sharp peak in the NS mass distribution suppresses support for heavy NS

The width of the NS mass peak, controlled by  $\sigma_{\text{peak}}^{\text{NS}}$ , directly influences the inferred probability  $P(\text{NS})$ . This parameter determines how tightly the population of NS is clustered around  $1.4 M_{\odot}$ . Variations in  $\sigma_{\text{peak}}^{\text{NS}}$  can either increase or decrease  $P(\text{NS})$ . To capture this non-monotonic behavior, we consider three representative cases for  $\sigma_{\text{peak}}^{\text{NS}}$ : narrow, intermediate, and broad, corresponding to increasingly wider NS mass distributions.

**Extremely narrow peak.** When  $\sigma_{\text{peak}}^{\text{NS}}$  is very small, the peak is sharply concentrated near  $1.4 M_{\odot}$ ,  $P(\text{NS})$  for GW230529’s primary and GW190425’s primary are relatively lower. In the  $q - m_1$  plane (Figure 4), this suppresses support at very low  $m_1$  and collapses the credible regions toward low  $q$ . In the  $q - m_2$  plane, contours tighten toward lower  $m_2$ . As shown in Figure 6, this

region has a comparatively low  $P(\text{NS})$  for GW190425’s primary. A detailed treatment of the  $m_1-m_2$  relation for this event appears in Foley et al. [101].

**Intermediate width.** As  $\sigma_{\text{peak}}^{\text{NS}}$  is increased to the point that the mass distribution begins to influence the NS-BH boundary region ( $\sim 2 - 3 M_{\odot}$ ), the broadening NS peak pulls  $m_1$  downward toward  $1.4 M_{\odot}$ . This shifts support away from the boundary and toward a confident NS, raising  $P(\text{NS})$ .

**Very broad peak (quasi-uniform).** If  $\sigma_{\text{peak}}^{\text{NS}}$  is so large that the peak approaches a near uniform distribution, the probability leaks into masses beyond  $\gamma_{\text{low}}$  (and  $m_{\text{max}}^{\text{EOS}}$ ), which lowers  $P(\text{NS})$ . Given the current state of observations, such an extremely wide NS mass distribution is disfavored.

Although the NS mass peak is strongly concentrated near  $1.4 M_{\odot}$  [102] and large shifts are unlikely, we vary  $\mu_{\text{peak}}^{\text{NS}}$  for completeness. The variability is weaker than  $\beta_{\text{LL}}$  and  $\sigma_{\text{peak}}^{\text{NS}}$ , and sizable shifts are astrophysically disfavored, so we do not pursue it further.

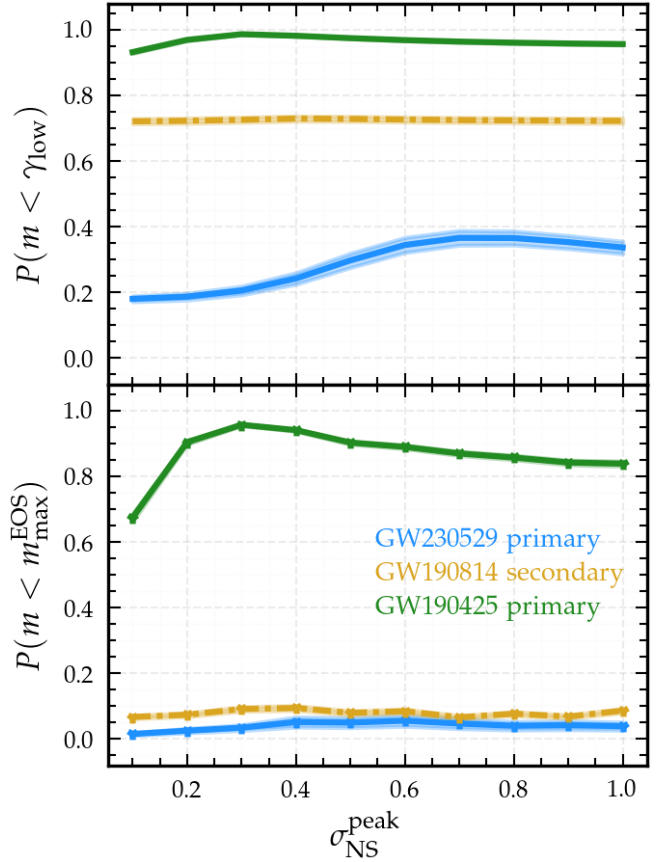


FIG. 6. Effect of the NS peak width,  $\sigma_{\text{peak}}^{\text{NS}}$ , on  $P(\text{NS})$ . **(Top)** Population-only,  $P(m < \gamma_{\text{low}})$ . **(Bottom)** EOS-informed,  $P(m < m_{\text{max}}^{\text{EOS}})$ . Extremely narrow peaks suppress heavy NS support. Refer to Sec IV D for a detailed explanation of the non-monotonic behavior in GW190425’s primary for  $P(m < m_{\text{max}}^{\text{EOS}})$ . The shaded region represents 90% credible interval around the mean. Primaries are solid lines and secondaries are dotted lines.

## V. THE $q - \chi_{\text{eff}}$ PLANE

We next examine the coupling between mass ratio  $q$  and effective spin  $\chi_{\text{eff}}$ , focusing on how spin properties influence  $P(\text{NS})$ . To disentangle these effects, we treat spin tilts and spin magnitudes separately. Figure 7 varies the mean spin tilt  $\mu_{\cos\theta}^{\text{low}}$ , while Figures 8 and 9 explore the mean spin magnitude  $\mu_{\chi}^{\text{low}}$  and its width  $\sigma_{\cos\theta}^{\text{low}}$ , respectively. As summarized in Table I, spin tilts produce comparable shifts to  $P(\text{NS})$  as spin magnitudes with the most pronounced responses arising in low SNR events where the  $q - \chi_{\text{eff}}$  degeneracy is broad.

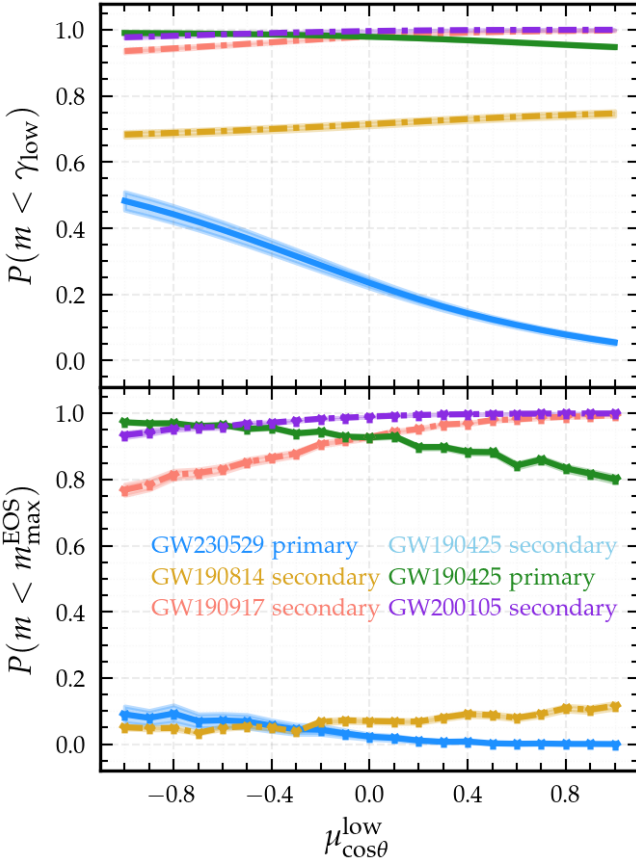


FIG. 7. Effect of the NS spin tilt mean  $\mu_{\cos\theta}^{\text{low}}$  on  $P(\text{NS})$ . (**Top**) Population-only,  $P(m < \gamma_{\text{low}})$ . (**Bottom**) EOS-informed,  $P(m < m_{\text{max}}^{\text{EOS}})$ . Notably, GW230529 (top blue) decreases by 43%. The shaded region represents 90% credible interval around the mean. Primaries are solid lines and secondaries are dotted lines.

### A. Spin tilts strongly vary $P(\text{NS})$ and shift primaries and secondaries in opposite directions

The Gaussian component of the spin tilt mixture, characterized by its mean  $\mu_{\cos\theta}^{\text{low}}$  and width  $\sigma_{\cos\theta}^{\text{low}}$ , may influence the apparent coupling between the mass ratio  $q$  and effective spin  $\chi_{\text{eff}}$ , which is determined by the likelihood.

Figures 4 and 7 illustrate this effect: increasing  $\mu_{\cos\theta}^{\text{low}}$  toward completely aligned (+1) favors larger  $\chi_{\text{eff}}$ . Because  $q$  and  $\chi_{\text{eff}}$  are anticorrelated, increasing  $\chi_{\text{eff}}$  pushes the reweighted posterior toward more asymmetric mass ratios (smaller  $q$ ), raising  $m_1$  and lowering  $m_2$  (see Figure 4).

The classification response in Figure 7 follows directly from this. For primaries, greater alignment (larger  $\mu_{\cos\theta}^{\text{low}}$ ) drives  $m_1$  upward, pushing it past the NS boundary and lowering  $P(\text{NS})$ . For secondaries, greater alignment (larger  $\mu_{\cos\theta}^{\text{low}}$ ) drives  $m_2$  downward, pulling it deeper into the NS range and raising  $P(\text{NS})$ .

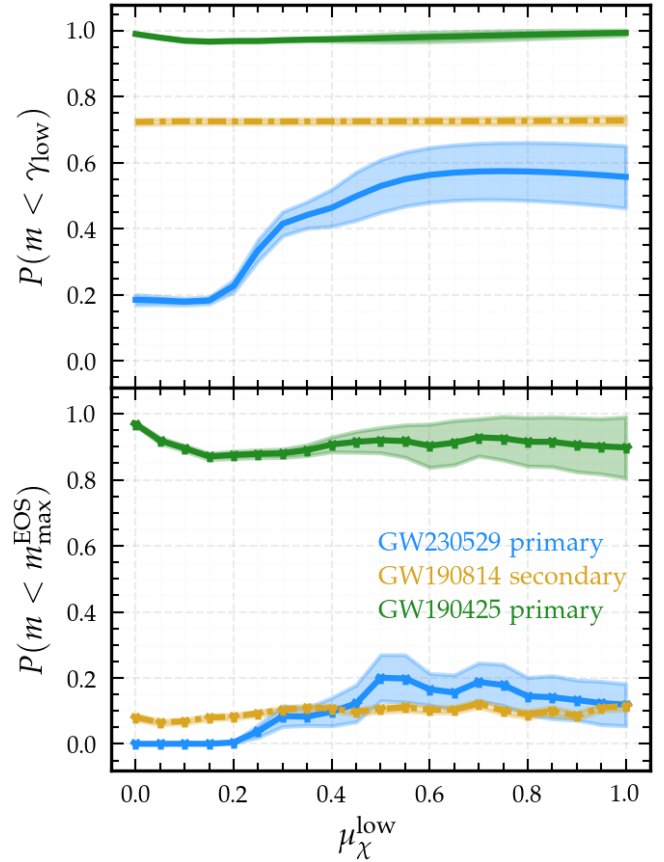


FIG. 8. Effect of the NS mean spin magnitude  $\mu_{\chi}^{\text{low}}$  on classification. (**Top**) Population-only,  $P(m < \gamma_{\text{low}})$ . (**Bottom**) EOS-informed,  $P(m < m_{\text{max}}^{\text{EOS}})$ . The shaded region represents 90% credible interval around the mean. Primaries are solid lines and secondaries are dotted lines.

### B. Spin magnitudes also strongly vary $P(\text{NS})$

The effect of varying the mean spin magnitude  $\mu_{\chi}^{\text{low}}$  for NS containing binaries is shown in Figure 8. Compared to  $\mu_{\cos\theta}^{\text{low}}$ , the impact on  $P(\text{NS})$  is also strong. The clearest trend arises in GW230529's primary. Increasing  $\mu_{\chi}^{\text{low}}$  raises  $\chi_{\text{eff}}$ , which couples to  $q$  through the  $q - \chi_{\text{eff}}$  anti-correlation, leading to higher  $P(\text{NS})$ .

The EOS-informed panel of Figure 8 confirms this picture, with a strong feature seen in GW190425’s primary. Here, the combination of low SNR and masses lying close to  $m_{\max}^{\text{EOS}}$  makes  $P(\text{NS})$  sensitive to  $\mu_{\chi}^{\text{low}}$ . At very low  $\mu_{\chi}^{\text{low}}$ , the effective spin is driven toward 0, which pushes  $q$  toward symmetry, raising  $P(\text{NS})$ . However, once  $\mu_{\chi}^{\text{low}}$  is allowed to deviate from 0,  $\chi_{\text{eff}}$  rises, which drives  $q$  to smaller values and correspondingly lowers  $P(\text{NS})$ . Figure 8 also shows that, at high  $\mu_{\chi}^{\text{low}}$ , low SNR events exhibit broader classification uncertainties. This arises from limited posterior support in the high spin magnitude subspace, where the scarcity of samples inflates the credible intervals.

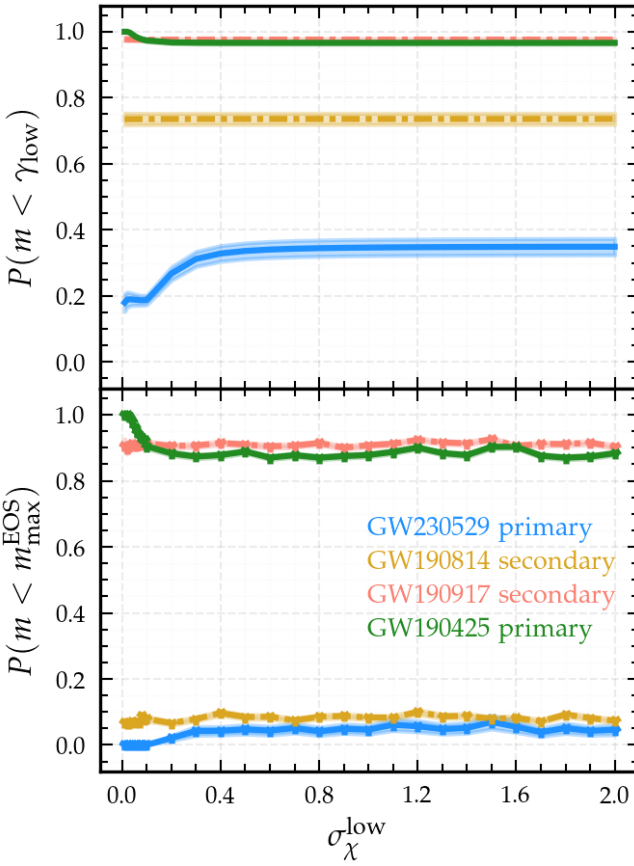


FIG. 9. Effect of NS spin magnitude width,  $\sigma_{\chi}^{\text{low}}$  on classification  $P(\text{NS})$ . (**Top**) Population-only,  $P(m < \gamma_{\text{low}})$ . (**Bottom**) EOS-informed,  $P(m < m_{\max}^{\text{EOS}})$ . The shaded region represents 90% credible interval around the mean. Primaries are solid lines and secondaries are dotted lines.

We now vary the width of the spin magnitude distribution  $\sigma_{\chi}^{\text{low}}$ . Across both the population-only and EOS-informed analyses, the resulting classifications are generally flat, with the only notable deviation occurring for GW190425 in the EOS panel when spin magnitudes are sharply peaked. For all other sources, broadening or narrowing  $\sigma_{\chi}^{\text{low}}$  leaves  $P(\text{NS})$  essentially unchanged (see Figure 9).

Taken together, Figures 7–9 show that spin magni-

tudes and tilts have a comparable influence on classification outcomes. Both sets of parameters can shift  $P(\text{NS})$  especially when event posteriors remain broad. Adjusting  $\mu_{\cos\theta}^{\text{low}}$  can shift  $P(\text{NS})$  substantially (ranging from 5% to 48% for GW230529’s primary and from 80% to 97% for GW190425’s primary), with the largest changes occurring in low SNR sources. Spin magnitude ( $\mu_{\chi}^{\text{low}}$  and  $\sigma_{\chi}^{\text{low}}$ ) produce similar shifts, most clearly visible in the population-only GW230529’s primary (ranging from 18% to 57%) and the EOS-informed GW190425’s primary (ranging from 87% to 97%). Owing to its weaker observational constraints,  $\mu_{\cos\theta}^{\text{low}}$  represents a more plausible driver of changes in  $P(\text{NS})$  than  $\mu_{\chi}^{\text{low}}$  [81]. For this reason, we choose  $\mu_{\cos\theta}^{\text{low}}$  as the (marginally) more important spin parameter in assessing classification sensitivity.

### C. Jointly changing $\mu_{\cos\theta}^{\text{low}}$ and $\beta_{\text{LL}}$ maximally varies $P(\text{NS})$

Having examined each parameter in isolation, we now “throw caution to the wind” and simultaneously change two hyperparameters that strongly impact classification: the NS spin tilt mean ( $\mu_{\cos\theta}^{\text{low}}$ ) and the BNS pairing exponent ( $\beta_{\text{LL}}$ ). Specifically, we compare two extrema for primaries:  $\beta_{\text{LL}} = 5$ ,  $\mu_{\cos\theta}^{\text{low}} = -1$  versus  $\beta_{\text{LL}} = -5$ ,  $\mu_{\cos\theta}^{\text{low}} = 1$ . For secondaries, we flip the sign of  $\beta_{\text{LL}}$ , because the  $(q, \chi_{\text{eff}})$ - $m_2$  correlation has the opposite sign to the  $(q, \chi_{\text{eff}})$ - $m_1$  correlation. These two choices approximately bound the largest possible change to  $P(\text{NS})$ , and the impact is dramatic. GW190425’s primary sweeps from 51% – 100%, representing the largest shift observed across all EOS-informed cases. Under the population-only case, the GW230529 primary exhibits the greatest variance, spanning 1% – 67%. Similarly, the EOS case for GW230529 still permits a substantial deviation of 0% to 21%. By construction, these settings align (or misalign) spins while simultaneously favoring equal-mass (versus asymmetric pairings). These extremes set an envelope on the impact of uncertainty in the population.

## VI. LOOKING AHEAD

For the EOS-dependent case, NS classification near the NS-BH boundary is inherently two-dimensional. The physical boundary is set jointly by the EOS-dependent maximum mass and its spin (which can affect the maximum mass through Equation 7). Hence, we operate in the joint  $(m_{\max}^{\text{EOS}}, \chi_{\max}^{\text{EOS}})$  plane rather than just the one dimensional  $m_{\max}^{\text{EOS}}$  cut. Accordingly, Figure 10 shows this space. This representation shows which dimension (mass or spin) has a stronger effect on  $P(\text{NS})$ . Reweighting primarily shifts probability along the  $m/m_{\max}^{\text{EOS}}$  axis, moving support from the shaded “Not NS” region into the “NS” region, while producing little change along  $\chi/\chi_{\max}$ . For realistic EOS,  $m_{\max}^{\text{EOS}}$  increases only weakly with spin, and the observed NS spins are either small or recover the prior

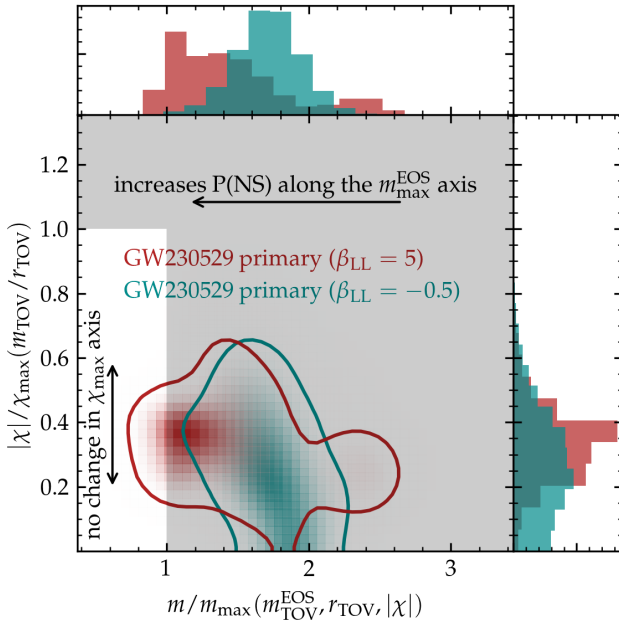


FIG. 10. EOS-informed reweighting for GW230529, comparing a strong preference for equal mass pairing ( $\beta_{\text{LL}} = 5$ , red) with a weak preference for equal mass pairing ( $\beta_{\text{LL}} = -0.5$ , green). Both hyperparameter choices are equally likely. Reweighting shifts support along the  $m/m_{\text{max}}$  axis, moving the support from shaded “Not NS” region into the “NS” region. In contrast, little change is seen along the  $|\chi|/\chi_{\text{max}}$  axis, indicating that variations in  $P(\text{NS})$  are largely influenced through the EOS-informed maximum-mass rather than spin.

(see Figure 3). As a result, we do not expect the spins to greatly alter the reweighted population, exactly what is observed in Figure 10. For the maximum spin to have an effect, we will need to measure NS mergers with much larger spins.

Having varied the population while holding the distribution over NS EOS fixed (using draws from Landry et al. [74]), a natural next step is to test different families of candidate EOS as a distribution over its physics [69–77]. This framework could extend the analysis of Essick and Landry [82], which examined GW190814 by systematically varying the EOS to assess whether it’s secondary could be consistent with a NS (see their Table 2). Such studies are motivated by current constraints leaving a wide plausible range of mass-radius relations, which directly influence the maximum NS mass and, consequently, the value of  $P(\text{NS})$ .

Beyond varying the EOS itself, another valuable extension could be to examine how alternative approaches to identifying the low-mass boundary of the population influence classification. For a first attempt, see Appendix E.

With relatively few BNS detections, the population of low-mass mergers remains fairly uncertain and variability in  $P(\text{NS})$  remains broad. As detections increase in forthcoming observing runs, high SNR (and asymmet-

ric) mergers will better constrain the NS population distribution, which will reduce the variability of  $P(\text{NS})$  for all events.

## VII. CONCLUSION

NS classification from GW observations is governed by assumptions about the CBC population, the EOS, and single-event measurement uncertainties. In both the population-only and EOS-informed analyses, the low mass compact object pairing ( $\beta_{\text{LL}}$ ), the NS spin tilt distribution ( $\mu_{\cos\theta}^{\text{low}}$ ) and the spin magnitude distribution ( $\mu_{\chi}^{\text{low}}$  and  $\sigma_{\chi}^{\text{low}}$ ) are the dominant parameters in shifting the inferred NS probability,  $P(\text{NS})$ . By comparison, other hyperparameters move  $P(\text{NS})$  moderately. Low SNR sources near the NS-BH boundary are the most sensitive to changes in classification. For example, under the population-only analysis, GW230529’s primary classification probability spans 1% – 67%, demonstrating the joint effects of  $\beta_{\text{LL}}$  and  $\mu_{\cos\theta}^{\text{low}}$ . Using an EOS-informed approach, GW190425’s primary varies from 51% – 100%. However, high-SNR asymmetric systems like GW190814 yield a  $P(\text{NS})$  that changes by  $\leq 10\%$ , indicating robustness to assumptions in the CBC population.

Looking ahead, three directions flow naturally. First, place greater confidence in classifications derived from low-mass, high-SNR signals, where the tighter posteriors reduce sensitivity to prior assumptions. Second, when reporting classification metrics such as  $P(\text{NS})$ , include an explicit uncertainty budget that surveys many population priors. Third, quantify how alternative EOS models modify  $P(\text{NS})$  by repeating the analysis under multiple EOS prescriptions, for many events. Collectively, these steps promote more robust classifications near the low-mass gap boundary.

Ultimately, reliable NS classifications depend on confronting population model dependencies head on. As multi-detector observations of NS mergers accumulate, they will naturally refine the demographics of spin magnitudes, tilt angles, and mass ratios, and map detection rates across the low-mass gap. With these advances,  $P(\text{NS})$  will enable more confident interpretation of future GW observations.

## ACKNOWLEDGMENTS

U.M. thanks Aditya Vijayumar, Sylvia Biscoveanu and Claire Ye for useful discussions.

U.M. and R.E thank Mike Zevin for reviewing the manuscript within the LVK.

U.M. and R.E are supported by the Natural Sciences & Engineering Research Council of Canada (NSERC) through a Discovery Grant (RGPIN-2023-03346).

This material is based upon work supported by NSF’s LIGO Laboratory which is a major facility fully funded by the National Science Foundation.

We also wish to acknowledge the land on which the University of Toronto operates. For thousands of years it has been the traditional land of the Huron-Wendat, the Seneca, and the Mississaugas of the Credit. Today,

this meeting place is still the home to many Indigenous people from across Turtle Island and we are grateful to have the opportunity to work on this land.

## Appendix A: Population Model

We model the population distribution as a product of contributions from the component masses, spins, and redshift. Our framework extends the FULLPOP4.0 model [81], which builds on earlier formulations introduced by Fishbach et al. [40], Farah et al. [61], and Mali and Essick [80]. This extension incorporates flexible features in the mass spectrum (power laws, peaks, and notches), mass-dependent spin prescriptions, and a redshift distribution that fits the evolving star formation rate. Together, these ingredients provide a unified hierarchical model for the CBC population.

We begin by factorizing our model into contributions from the redshift distribution, the joint mass distribution, and the spin distributions:

$$p(\theta|\Lambda) = p(z|\Lambda)p(m_1, m_2|\Lambda)p(s_2|m_2, \Lambda)p(s_1|m_1, \Lambda) \quad (\text{A1})$$

We will now explain our mass, spin and distance models separately.

### 1. Joint Mass Distribution

The joint mass distribution is expressed as a product of two mass distributions together with a pairing function,

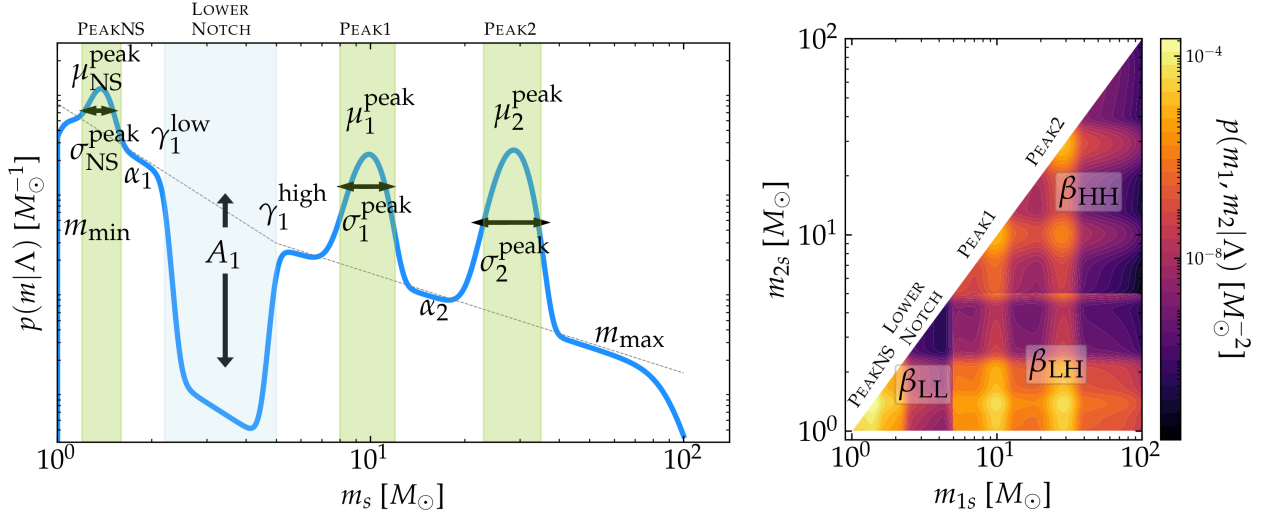


FIG. 11. (Left) Illustration of the one-dimensional mass distribution  $p(m|\Lambda)$  (Eq. A4) and its hyper-parameters. The baseline broken power law (dotted) extends between  $m_{\min}^{\text{model}}$  and  $m_{\max}^{\text{model}}$  (where the model tapers below  $m_{\min}$  and above  $m_{\max}$ ) with roll-offs  $\gamma_{\text{low},\text{high}}$ . Gaussian peaks (green) represent localized excesses (e.g. NS peak, black hole peaks), while Butterworth notch filters (blue) carve deficits. (Right) The corresponding joint distribution  $p(m_1, m_2|\Lambda)$  (Eq. A2), where pairing hyper-parameters  $\beta_{\text{LL}}$ ,  $\beta_{\text{LH}}$ , and  $\beta_{\text{HH}}$  outline support across the Low-Low, Low-High, and High-High compact object ranges. Features in  $p(m|\Lambda)$  imprint symmetrically on both  $m_1$  and  $m_2$ .

$$p(m_1, m_2|\Lambda) = p(m_1|\Lambda)p(m_2|\Lambda)f(m_1, m_2, \beta_{\text{LL}}, \beta_{\text{HH}}, \beta_{\text{LH}}) \quad (\text{A2})$$

We consider a three-pronged pairing function with a separate pairing powerlaw for Low-Low, Low-High and High-High compact mergers ( $\beta_{\text{LL}}$ ,  $\beta_{\text{HH}}$ ,  $\beta_{\text{LH}}$ ). The three pairing function is given by:

$$f(m_{1s}, m_{2s}, \beta_{LL}, \beta_{HH}, \beta_{LH}) = \begin{cases} \left(\frac{m_{2s}}{m_{1s}}\right)^{\beta_{LL}} & \text{if } m_{2s} < 5M_{\odot} \text{ and } m_{1s} < 5M_{\odot} \text{ (Low-Low)} \\ \left(\frac{m_{2s}}{m_{1s}}\right)^{\beta_{LH}} & \text{if } m_{1s} \geq 5M_{\odot} \text{ and } m_{2s} \leq 5M_{\odot} \text{ (Low-High)} \\ \left(\frac{m_{2s}}{m_{1s}}\right)^{\beta_{HH}} & \text{if } m_{2s} \geq 5M_{\odot} \text{ and } m_{1s} \geq 5M_{\odot} \text{ (High-High)} \end{cases} \quad (\text{A3})$$

The latent mass spectrum (in the source frame, i.e.  $m_{1s}, m_{2s}$ ) incorporates a broken power law with flexible low and high mass cutoffs, Gaussian peaks, and notches (dips) to model over- and under-densities:

$$\begin{aligned} p(m|\Lambda) &= \left[ 1 + c_1 \mathcal{N}_{[m_{\min}, m_{\max}]}(m | \mu_1, \sigma_1) + c_2 \mathcal{N}_{[m_{\min}, m_{\max}]}(m | \mu_2, \sigma_2) + c_{\text{NS}} \mathcal{N}_{[m_{\min}, m_{\max}]}(m | \mu_{\text{NS}}, \sigma_{\text{NS}}) \right] \\ &\times n(m|\gamma_{\text{low}}, \gamma_{\text{high}}, \eta_{\text{low}}, \eta_{\text{high}}, A) \\ &\times h(m|m_{\max}, \eta_{\min}) \times \ell(m|m_{\max}, \eta_{\max}) \\ &\times \begin{cases} \left(\frac{m}{m_{\text{break}}}\right)^{\alpha_1}, & m < m_{\text{break}}, \\ \left(\frac{m}{m_{\text{break}}}\right)^{\alpha_2}, & m \geq m_{\text{break}}, \end{cases} \\ &\times \begin{cases} 1, & m_{\min}^{\text{model}} \leq m \leq m_{\max}^{\text{model}} \\ 0, & \text{otherwise} \end{cases} \end{aligned} \quad (\text{A4})$$

where  $n(m)$  denotes the notch component,  $h(m)$  and  $\ell(m)$  are highpass and lowpass filters, and  $\mathcal{N}_{[a,b]}$  are truncated Gaussians. Specifically, we use

$$\ell(m|k, \eta) = (1 + (m/k)^{\eta})^{-1} \quad (\text{A5})$$

$$h(m|k, \eta) = 1 - \ell(m|k, \eta) \quad (\text{A6})$$

which smoothly turn the distribution off at characteristic scales  $k$  with sharpness controlled by  $\eta$ . Localized dips or chips in the spectrum, such as the lower and upper notches shown in Figure 11, are modeled through

$$n(m|\gamma_{\text{low}}, \gamma_{\text{high}}, \eta_{\text{low}}, \eta_{\text{high}}, A) = 1 - A h(m|\gamma_{\text{low}}, \eta_{\text{low}}) \ell(m|\gamma_{\text{high}}, \eta_{\text{high}}) \quad (\text{A7})$$

where the parameters set the edges, widths, and depth of the dip.

In addition to power law components and notches, we allow for Gaussian peaks. These are implemented with truncated normal distributions to ensure support only within specific bounds  $[a, b]$ :

$$\mathcal{N}_{[a,b]} f(m | \mu, \sigma) = \begin{cases} \frac{\exp\left[-\frac{1}{2} \left(\frac{m-\mu}{\sigma}\right)^2\right]}{\frac{1}{2} \sigma \sqrt{2\pi} \left[\text{erf}\left(\frac{b-\mu}{\sqrt{2}\sigma}\right) - \text{erf}\left(\frac{a-\mu}{\sqrt{2}\sigma}\right)\right]}, & a \leq m \leq b \\ 0, & \text{otherwise} \end{cases} \quad (\text{A8})$$

Tables III and IV summarize the parameters governing the mass model and the pairing function. Figure 11 illustrates the structure of the mass model. The left panel shows how the low and high mass cutoffs, broken power law, Gaussian peaks, and notches combine. The right panel shows the resulting joint mass distribution, highlighting the role of the separate pairing functions for BNS, NSBH, and BBH sectors.

## 2. Mass-dependent Spin Distribution

In addition to masses, the distribution of spin magnitudes and orientations plays a key role in the population. We model the spin degrees of freedom as conditionally independent given their component masses,

$$p(s_1, s_2 | m_1, m_2, \Lambda) = \left[ p(\chi_1 | m_1, \Lambda) p(\cos \theta_1 | m_1, \Lambda) \right] \left[ p(\chi_2 | m_2, \Lambda) p(\cos \theta_2 | m_2, \Lambda) \right]. \quad (\text{A9})$$

TABLE III. Summary of FULLPOP-4.0 mass population (and extensions) parameters and priors.

Category	Parameter	Unit	Description	Prior
Broken Power-Law	$\alpha_1$	–	Power-law slope below $m_{\text{break}}$	$U(-5, 5)$
	$\alpha_2$	–	Power-law slope above $m_{\text{break}}$	$U(-5, 5)$
	$m_{\text{break}}$	$M_{\odot}$	Break point between $\alpha_1$ and $\alpha_2$	$U(2, 10)$
Highpass Filter	$m_{\text{min}}$	$M_{\odot}$	Low-mass roll-on location	$U(1, 1.2)$
	$\eta_{\text{min}}$	–	Sharpness at $m_{\text{min}}$	$U(10, 50)$
Lowpass Filter	$m_{\text{max}}$	$M_{\odot}$	High-mass roll-off location	$U(35, 100)$
	$\eta_{\text{max}}$	–	Sharpness at $m_{\text{max}}$	$U(0, 10)$
Notch (gap)	$\gamma_{\text{low}}$	$M_{\odot}$	Lower notch edge	$U(2, 4)$
	$\eta_{\text{low}}$	–	Sharpness at $\gamma_{\text{low}}$	$U(0, 50)$
	$\gamma_{\text{high}}$	$M_{\odot}$	Upper notch edge	$U(4, 8)$
	$\eta_{\text{high}}$	–	Sharpness at $\gamma_{\text{high}}$	$U(0, 50)$
	$A_1$	–	Lower Notch depth (dip amplitude; negative permits a bump)	$U(-1, 1)$
Low-Mass Peak	$\mu_1^{\text{peak}}$	$M_{\odot}$	Peak location	$U(6, 12)$
	$\sigma_1^{\text{peak}}$	$M_{\odot}$	Peak width	$U(1, 40)$
	$c_1$	–	Peak height (amplitude)	$U(0, 500)$
High-Mass Peak	$\mu_2^{\text{peak}}$	$M_{\odot}$	Peak location	$U(20, 60)$
	$\sigma_2^{\text{peak}}$	$M_{\odot}$	Peak width	$U(1, 40)$
	$c_2$	–	Peak height (amplitude)	$U(0, 500)$
NS Peak	$\mu_{\text{peak}}^{\text{NS}}$	$M_{\odot}$	Peak location	$U(1.01, 2.3)$
	$\sigma_{\text{peak}}^{\text{NS}}$	$M_{\odot}$	Peak width	$U(0.1, 1)$
	$c_{\text{NS}}$	–	Peak height (amplitude)	$U(0, 1000)$
Model Bounds	$m_{\text{min}}^{\text{model}}$	$M_{\odot}$	Support lower bound	1
	$m_{\text{max}}^{\text{model}}$	$M_{\odot}$	Support upper bound	100

TABLE IV. Pairing function parameters and priors.

Category	Parameter	Unit	Description	Prior
Pairing Function	$\beta_{\text{LL}}$	–	Spectral index for systems in the BNS range; $(m_1, m_2 < m_{\text{sep}})$	$U(-5, 5)$
	$\beta_{\text{HH}}$	–	Spectral index for systems in the BBH range; $(m_1, m_2 > m_{\text{sep}})$	$U(-5, 5)$
	$\beta_{\text{LH}}$	–	Spectral index for systems in the NSBH range; $(m_2 < m_{\text{sep}} < m_1)$	$U(-5, 5)$
	$m_{\text{sep}}$	$M_{\odot}$	Separator mass for pairing regimes	5

This factorization separates the spin magnitudes ( $\chi$ ) and cosine of the tilt angles ( $\cos \theta$ ) and allows each to vary with the component mass. We implement a mass break at  $m_{\text{break,spin}} = 3M_{\odot}$  to distinguish between objects in the low and high mass ranges. Below this threshold, spin magnitudes have a reduced maximum value due to the limited coverage of the O3 injections [85]. The spin magnitude is split into a piecewise Gaussian,

$$p(\chi | m, \Lambda) = \begin{cases} \mathcal{N}_{[\chi_{\text{min}}, \chi_{\text{max}}]}(\chi | \mu_{\chi}^{\text{low}}, \sigma_{\chi}^{\text{low}}), & m < m_{\text{break,spin}}, \\ \mathcal{N}_{[\chi_{\text{min}}, \chi_{\text{max}}]}(\chi | \mu_{\chi}^{\text{high}}, \sigma_{\chi}^{\text{high}}), & m \geq m_{\text{break,spin}}, \end{cases} \quad (\text{A10})$$

where the means and widths of the truncated normals are separately parametrized above and below  $m_{\text{break,spin}}$ . Similarly, the tilt distributions is mass-dependent. Each is modeled as a mixture between an isotropic distribution and a truncated normal centered on alignment ( $\cos \theta \approx 1$ ):

$$p(\cos \theta | m, \Lambda) = \begin{cases} \lambda_{\cos \theta}^{\text{low}} \mathcal{N}_{[c_{\text{min}}, c_{\text{max}}]}(\cos \theta | 1, \sigma_{\cos \theta}^{\text{low}}) + (1 - \lambda_{\cos \theta}^{\text{low}}) \frac{1}{c_{\text{max}} - c_{\text{min}}}, & m < m_{\text{break,spin}} \\ \lambda_{\cos \theta}^{\text{high}} \mathcal{N}_{[c_{\text{min}}, c_{\text{max}}]}(\cos \theta | 1, \sigma_{\cos \theta}^{\text{high}}) + (1 - \lambda_{\cos \theta}^{\text{high}}) \frac{1}{c_{\text{max}} - c_{\text{min}}}, & m \geq m_{\text{break,spin}} \end{cases} \quad (\text{A11})$$

with  $c_{\text{max}} = \cos \theta_{\text{max}} = +1$  and  $c_{\text{min}} = \cos \theta_{\text{min}} = -1$  defining the support.

Table V summarizes the full set of hyperparameters and priors for the spin model.

TABLE V. Summary of mass dependent spin distribution parameters and priors. We denote a uniform distribution between X and Y as U(X, Y).

Category	Parameter	Description	Prior
Spin magnitude ( $m < m_{\text{break,spin}}$ )	$\mu_{\chi}^{\text{low}}$	Mean of truncated normal below $m_{\text{break,spin}}$	U(0, 0.4)
	$\sigma_{\chi}^{\text{low}}$	Std. dev. of truncated normal below $m_{\text{break,spin}}$	U(0.05, 2)
	$\chi_{\max}^{\text{low}}$	Upper bound on $\chi_i$	0.4
	$\chi_{\min}^{\text{low}}$	Lower bound on $\chi_i$	0
Spin magnitude ( $m \geq m_{\text{break,spin}}$ )	$\mu_{\chi}^{\text{high}}$	Mean of truncated normal above $m_{\text{break,spin}}$	U(0, 1)
	$\sigma_{\chi}^{\text{high}}$	Width of truncated normal above $m_{\text{break,spin}}$	U(0.05, 2)
	$\chi_{\max}^{\text{high}}$	Upper bound on $\chi_i$	1
	$\chi_{\min}^{\text{high}}$	Lower bound on $\chi_i$	0
Tilt ( $m < m_{\text{break,spin}}$ )	$\lambda_{\cos\theta}^{\text{low}}$	Mixture fraction for truncated normal component	U(0, 1)
	$\sigma_{\cos\theta}^{\text{low}}$	Width of truncated normal component	U(0.1, 4)
Tilt ( $m \geq m_{\text{break,spin}}$ )	$\lambda_{\cos\theta}^{\text{high}}$	Mixture fraction for truncated normal component	U(0, 1)
	$\sigma_{\cos\theta}^{\text{high}}$	Width of truncated normal component	U(0.1, 4)
Spin tilt support	$c_{\max}$	Upper bound on $\cos\theta$	1
	$c_{\min}$	Lower bound on $\cos\theta$	-1
Spin mass break	$m_{\text{break,spin}}$	Mass threshold separating the two spin regimes	$3M_{\odot}$

TABLE VI. Summary of redshift distribution parameters and cosmology. All cosmology parameters are fixed to Planck 2015.

Category	Parameter	Description	Prior
Cosmology	Rate Evolution $\kappa$	Redshift-evolution index	U(-4, 8)
	$H_0$	Present day expansion rate	$67.66 \text{ [km s}^{-1} \text{ Mpc}^{-1}\text{]}$
	$\Omega_{m,0}$	Matter density	0.311
	$\Omega_{r,0}$	Radiation density	0.001
	$\Omega_{k,0}$	Curvature density	0
	$\Omega_{\Lambda,0}$	Cosmological constant density	$1 - \Omega_{m,0} - \Omega_{r,0} - \Omega_{k,0}$
	$w$	Dark-energy equation-of-state	-1

### 3. Redshift Distribution

The final component of the population model describes the distribution of sources in redshift. This term accounts for the cosmological volume element, cosmological redshift, and rate-evolution as a function of cosmic time. We parameterize it as

$$p(z | H_0, \Omega_{m,0}, w, \kappa) \propto \frac{dV_c}{dz}(H_0, \Omega_{m,0}, w) \frac{1}{1+z} (1+z)^{\kappa} \quad (\text{A12})$$

where the comoving element is defined as

$$\frac{dV_c}{dz}(z | H_0, \Omega_{m,0}, w) = \frac{4\pi c}{H_0} \frac{d_L^2(z)}{E(z)(1+z)^2} \quad (\text{A13})$$

and the factor of  $(1+z)^{-1}$  in Equation A12 accounts for cosmological redshift, and the additional  $(1+z)^{\kappa}$  term allows for evolution in the merger rate. This form makes explicit the dependence on cosmology through  $H_0$ , the matter density  $\Omega_{m,0}$ , and the dark-energy equation of state  $w$ , defined as the ratio of pressure to energy density for dark energy. The function  $E(z)$  encapsulates how the cosmic expansion rate evolves with redshift and is determined by the fractional density parameters of the Universe today: matter ( $\Omega_{m,0}$ ), radiation ( $\Omega_{r,0}$ ), spatial curvature ( $\Omega_{k,0}$ ), and dark energy ( $\Omega_{\Lambda,0}$ ).

Together, these parameters determine the comoving volume. Table VI lists the parameters used in this redshift model. In our analysis, all cosmological parameters are fixed to the Planck 2015 values [103], while the redshift-evolution index  $\kappa$  is left free.

## Appendix B: GWTC-3.0 vs. GWTC-4.0

The expected impact of GWTC-4.0 on our conclusions is small. GWTC-4.0 does not add confirmed BNS events. Consequently, the parts of the population which control the NS mass, spin, and redshift distributions will remain anchored by the same information already present in GWTC-3.0. The dominant hyperparameters for  $P(\text{NS})$  in our framework are the BNS pairing at low masses ( $\beta_{\text{LL}}$ ) and the NS tilt mean ( $\mu_{\cos\theta}^{\text{low}}$ ). Although GWTC-4.0 highlights updates to the mean spin tilt distributions for BH, our populations treats BH and NS with separate tilt hyperparameters. As a result, we do not expect a great change to  $\mu_{\cos\theta}^{\text{low}}$ . For these reasons, we expect that updating our population inference to include GWTC-4.0 would not alter our main conclusions.

## Appendix C: Comparisons to the GW230529 exceptional event paper

When conducting our analysis, we attempted to reproduce the published GW230529 results from Abac et al. [17] and encountered some discrepancies. A thorough review revealed an error in the original classification code, which prevented the population parameters from being correctly updated when marginalizing over the hyperposterior. This only affects the quoted probabilities for the POWER LAW + DIP + BREAK model in Table 3 and the surrounding discussion in Abac et al. [17]. Correcting for this, we find that  $P(m_1 \text{ is NS})$  drops from  $8.8 \pm 2.8\%$  to  $4.2 \pm 0.7\%$  and  $P(m_2 \text{ is NS})$  increases from  $98.4 \pm 1.3\%$  to  $99.2 \pm 0.4\%$  when using the default spin assumptions (isotropic orientations and uniform in magnitude up to a maximum of 0.4). When these spin assumptions are relaxed and spin magnitudes can be as large as 0.99, we now find that  $P(m_1 \text{ is NS})$  only increases to  $13.1 \pm 0.7\%$  instead of to  $27.3 \pm 3.8\%$ .

While the exact classification probabilities change, they do not affect the key takeaways from Abac et al. [17]. Additionally, our analysis explores a much broader range of possible populations, and we find that the primary can still reach probabilities as large as  $\mathcal{O}(1 \text{ in } 2)$  in population-only analysis (see Section V C) and  $\mathcal{O}(1 \text{ in } 4)$  under specific EOS-informed choices (see Section IV C and V A). While such conclusions should not be overinterpreted, they nonetheless reinforce the original point presented in Abac et al. [17] that event classifications can depend strongly on poorly constrained aspects of the population of merging binaries.

## Appendix D: Classification of Neutron Stars - Monte Carlo Uncertainty

We now describe the Monte Carlo sums used to estimate  $P(\text{NS})$  throughout our study. For individual events with data  $d_i$ , we use posterior samples constructed using a reference population model  $\Lambda_{\text{ref}}$ :

$$p(\theta|d_i, \Lambda_{\text{ref}}) = \frac{p(d_i|\theta) p(\theta|\Lambda_{\text{ref}})}{p(d_i|\Lambda_{\text{ref}})} \quad (\text{D1})$$

We then use importance sampling to evaluate integrals over  $\theta$ . Given  $M$  samples  $\theta_k$  drawn from  $p(\theta|d, \Lambda_{\text{ref}}, H)$  with weights  $W_k$ , the expectation value over a function  $F(\theta)$  is approximated as:

$$\int d\theta p(\theta|d, \Lambda_{\text{ref}}, H) F(\theta) \approx \frac{1}{M} \sum_{k=1}^M W_k F(\theta_k) \quad (\text{D2})$$

When evaluating the same function under a different population model  $\Lambda$ , we reweight the samples via:

$$\int d\theta p(\theta|d, \Lambda, H) F(\theta) \approx \left( \sum_{k=1}^M w_k(\Lambda) \right)^{-1} \sum_{k=1}^M w_k(\Lambda) F(\theta_k) \quad (\text{D3})$$

with

$$\omega_k(\Lambda) = W_k \frac{p(\theta_k|\Lambda, H)}{p(\theta_k|\Lambda_{\text{ref}}, H)} \quad (\text{D4})$$

Referring back to Equation 8, the outer integral over  $\Lambda$  and EOS is approximated with  $N$  samples  $(\Lambda_p, \epsilon_p)$  with weights  $\omega_p$ :

$$\int d\Lambda d\text{EOS} p(\Lambda, \text{EOS}|H) F(\Lambda, \text{EOS}) \approx \left( \sum_{p=1}^N \omega_p \right)^{-1} \sum_{p=1}^N \omega_p F(\Lambda_p, \text{EOS}_p) \quad (\text{D5})$$

Combining these expressions, we estimate the probability that an object is consistent with a NS as:

$$P(\text{NS}) = \frac{1}{\sum_p^N \omega_p} \sum_p^N \left[ \frac{\omega_p}{\sum_k^M \omega_k(\Lambda_p)} \sum_k^M [\omega_k(\Lambda_p) \Theta_{\text{NS}}(\theta_k | \varepsilon_p)] \right] \quad (\text{D6})$$

where  $\varepsilon_p$  is the inferred population ( $\Lambda_p$ ) in the population-only case and the combined population in the EOS-informed case ( $\Lambda_p, \varepsilon_p$ ). We separate Eq. D6 into four pieces and compute the moments of each in turn. Specifically, we define

$$\hat{\mathcal{P}} = \frac{F}{G} \quad (\text{D7})$$

where

$$G = \frac{1}{N} \sum_p^N \omega_p \quad (\text{D8})$$

$$F = \frac{1}{N} \sum_p^N \omega_p \frac{f(\Lambda_p, \varepsilon_p)}{g(\Lambda_p)} \quad (\text{D9})$$

and

$$g(\Lambda) = \frac{1}{M} \sum_k^M w_k(\Lambda) \quad (\text{D10})$$

$$f(\Lambda, \varepsilon) = \frac{1}{M} \sum_k^M w_k(\Lambda) \Theta_{\text{NS}}(\theta_k | \varepsilon) \quad (\text{D11})$$

We compute moments (expectation values  $E[\cdot]_x$ , variances  $V[\cdot]_x$ , and/or covariances  $C[\cdot, \cdot]_x$ ) of each under the measures associated with drawing samples  $x$  (either  $\theta_k \sim p(\theta)$  and  $\Lambda_p, \varepsilon_p \sim p(\Lambda, \varepsilon)$ ). We then approximate the moments of the ratio assuming the uncertainty in each sum is small

$$E\left[\frac{a}{b}\right]_x \approx \frac{E[a]_x}{E[b]_x} \quad (\text{D12})$$

$$V\left[\frac{a}{b}\right]_x \approx \frac{1}{E[b]_x^2} V[a]_x + \frac{E[a]_x^2}{E[b]_x^4} V[b]_x - \frac{2E[a]_x}{E[b]_x^3} C[a, b]_x \quad (\text{D13})$$

which comes from approximating errors as Gaussian and expanding the ratio to first order in terms of small errors away from the expected values.

### 1. Monte Carlo uncertainty from sums over single-event uncertainty

Now, one can compute moments of Monte Carlo sums by integrating over the measure that defines how the samples were drawn

$$\begin{aligned} E[g]_\theta &= \int \prod_\kappa^M d\theta_\kappa p(\theta_\kappa) \left( \frac{1}{M} \sum_k^M w_k \right) \\ &= \int d\theta p(\theta) w(\theta, \Lambda) \end{aligned} \quad (\text{D14})$$

Similarly, by computing the second moment of  $g$ , we obtain

$$V[g]_\theta = \frac{1}{M} \left( \int d\theta p(\theta) w(\theta, \Lambda)^2 - \left( \int d\theta p(\theta) w(\theta, \Lambda) \right)^2 \right) \quad (\text{D15})$$

We can approximate both these moments with sums over the samples  $\theta_k \sim p(\theta)$

$$\mathbb{E}[g]_\theta \approx \frac{1}{M} \sum_k^M w_k(\Lambda) \quad (\text{D16})$$

$$\mathbb{V}[g]_\theta \approx \frac{1}{M} \left( \left[ \frac{1}{M} \sum_k^M w_k^2 \right] - \mathbb{E}[g]_\theta^2 \right) \quad (\text{D17})$$

We also obtain estimates for the moments of  $f$

$$\mathbb{E}[f]_\theta \approx \frac{1}{M} \sum_k^M w_k \Theta_k \quad (\text{D18})$$

$$\mathbb{V}[f]_\theta \approx \frac{1}{M} \left( \left[ \frac{1}{M} \sum_k^M w_k^2 \Theta_k \right] - \mathbb{E}[f]_\theta^2 \right) \quad (\text{D19})$$

where  $\Theta_k = \Theta_{\text{NS}}(\theta_k | \varepsilon)$  and

$$\mathbb{C}[f, g]_\theta \approx \frac{1}{M} \left( \left[ \frac{1}{M} \sum_k^M w_k^2 \Theta_k \right] - \mathbb{E}[f]_\theta \mathbb{E}[g]_\theta \right) \quad (\text{D20})$$

Noting that these moments depend on both  $\Lambda$  and  $\varepsilon$ , one can approximate  $\mathbb{E}[f/g]_\theta$  and  $\mathbb{V}[f/g]_\theta$  for each sample  $(\Lambda_p, \varepsilon_p)$  separately via Eqs. D12 and D13.

## 2. Monte Carlo uncertainty from sums over population uncertainty

We now consider the uncertainty from the finite number of population samples. Following a similar procedure as Sec. D 1, it is straightforward to show that

$$\mathbb{E}[G]_{\Lambda, \varepsilon} \approx \frac{1}{N} \sum_p^N \omega_p \quad (\text{D21})$$

$$\mathbb{V}[G]_{\Lambda, \varepsilon} \approx \frac{1}{N} \left( \left[ \frac{1}{N} \sum_p^N \omega_p^2 \right] - \mathbb{E}[G]_{\Lambda, \varepsilon}^2 \right) \quad (\text{D22})$$

The moments of  $F$  are slightly more complicated, but it is also possible to show that

$$\mathbb{E}[F]_{\Lambda, \varepsilon, \theta} \approx \frac{1}{N} \sum_p^N \omega_p \mathbb{E} \left[ \frac{f_p}{g_p} \right]_\theta \quad (\text{D23})$$

where  $f_p = f(\Lambda_p, \varepsilon_p)$  and  $g_p = g(\Lambda_p)$ . One can also show that

$$\mathbb{E}[F^2]_{\Lambda, \varepsilon, \theta} \approx \frac{1}{N} \left( \frac{1}{N} \sum_p^N \omega_p^2 \mathbb{E} \left[ \left( \frac{f_p}{g_p} \right)^2 \right]_\theta \right) + \left( 1 - \frac{1}{N} \right) \frac{1}{N^2} \sum_p^N \omega_p \sum_q^N \omega_q \mathbb{E} \left[ \frac{f_p}{g_p} \frac{f_q}{g_q} \right]_\theta \quad (\text{D24})$$

Expanding the moments with respect to  $\theta$  in terms of expected values and (co)variances yields

$$\begin{aligned} \mathbb{V}[F]_{\Lambda, \varepsilon, \theta} &\approx \frac{1}{N} \left( \left[ \frac{1}{N} \sum_p^N \omega_p^2 \mathbb{E} \left[ \left( \frac{f_p}{g_p} \right)^2 \right]_\theta \right] - \mathbb{E}[F]_{\Lambda, \varepsilon, \theta}^2 \right) \\ &+ \left( 2 - \frac{1}{N} \right) \frac{1}{N^2} \sum_p^N \omega_p^2 \mathbb{V} \left[ \frac{f_p}{g_p} \right]_\theta \\ &+ \left( 1 - \frac{1}{N} \right) \frac{1}{N^2} \sum_p^N \omega_p \sum_{q \neq p}^N \omega_q \mathbb{C} \left[ \frac{f_p}{g_p} \frac{f_q}{g_q} \right]_\theta \end{aligned} \quad (\text{D25})$$

Let us interpret each of these terms in turn. The first term is the standard expression for the uncertainty in a Monte Carlo sum assuming the estimate  $E[f/g]_\theta$  is known exactly for each  $(\Lambda, \varepsilon)$  sample. The second and third lines account for the additional uncertainty from the fact that  $E[f/g]_\theta$  is not a perfect estimator. If one considers the second line by itself, this is proportional to the variance expected from adding  $N$  uncorrelated noisy estimators together, each with a weight  $\omega_p/N$ . This term will vanish as  $O(1/N)$  as the number of population samples increases. This is because, even if each individual estimator is noisy, the sum of a very large number of noisy estimators can still be a precise estimator. The third line, however, does not (in general) vanish as  $N \rightarrow \infty$ . This represents the residual uncertainty from the fact that we reuse the same single-event parameter samples for each population sample. In fact, this term scales as  $C[f_p f_q / g_p g_q]_\theta \sim O(1/M)$ .

One could estimate  $C[(f_p/g_p)(f_q/g_q)]_\theta$  directly for all pairs of population samples, but this scales as  $N(N+1)/2$  and may be extremely costly for large sample sizes. Instead, we consider the upper limit

$$\left| C \left[ \left( \frac{f_p}{g_p} \right) \left( \frac{f_q}{g_q} \right) \right]_\theta \right| \leq \sqrt{V \left[ \frac{f_p}{g_p} \right]_\theta V \left[ \frac{f_q}{g_q} \right]_\theta} \quad (\text{D26})$$

and obtain

$$\begin{aligned} V[F]_{\Lambda, \varepsilon, \theta} &\lesssim \frac{1}{N} \left( \frac{1}{N} \sum_p^N \omega_p^2 E \left[ \frac{f_p}{g_p} \right]^2_\theta - \left( \frac{1}{N} \sum_p^N \omega_p E \left[ \frac{f_p}{g_p} \right]_\theta \right)^2 \right) \\ &+ \frac{1}{N} \left( \frac{1}{N} \sum_p^N \omega_p^2 V \left[ \frac{f_p}{g_p} \right]_\theta - \left( \frac{1}{N} \sum_p^N \omega_p V \left[ \frac{f_p}{g_p} \right]^{1/2}_\theta \right)^2 \right) \\ &+ \left( \frac{1}{N} \sum_p^N \omega_p V \left[ \frac{f_p}{g_p} \right]^{1/2}_\theta \right)^2 \end{aligned} \quad (\text{D27})$$

Again, the first two lines vanish as  $O(1/N)$ , but the third line remains finite. This persistent term is an averaged uncertainty from the individual estimates derived from sums over single-event parameter uncertainty, and it corresponds to the variance in the sum of many perfectly correlated variates. Again, it will instead vanish as  $O(1/M)$ .

Finally, we can also approximate

$$C[F, G]_{\Lambda, \varepsilon, \theta} \approx \frac{1}{N} \left( \left[ \frac{1}{N} \sum_p^N \omega_p^2 E \left[ \frac{f_p}{g_p} \right]_\theta \right] - E[G]_\Lambda E[F]_{\Lambda, \varepsilon, \theta} \right) \quad (\text{D28})$$

With these expressions, we can then approximate  $\hat{P}$  and its uncertainty via Eqs. D12 and D13.

The expressions above are implemented within the publicly available library `mmax-model-selection` [98], which in turn depends on `gw-distributions` [99] for models of the astrophysical population. These libraries are lightweight and, for  $N \sim M \sim 1000$ , estimates of the prior/posterior probabilities, odds ratios, and the Bayes factor can be run on a laptop (a single Apple M3 Pro CPU clocked at 4.05 GHz) in  $O(15)$  sec.

## Appendix E: What about non-parametric mass models?

We intentionally do not deploy a non-parametric mass model here for two reasons. First, the core aim of this paper is interpretability: we wish to isolate how specific, physically meaningful population parameters (NS peak, pairing, spin magnitudes/tilts etc.) affect classification. Non-parametric models, while flexible, tend to absorb such effects into an overall feature making such connections opaque. Second, introducing a non-parametric layer to classification would add additional priors whose influence may rival the physics we seek to probe. This highlights a more general problem with the tradeoff between interpretable models which are highly parametrized and weakly parametrized models which lack interpretability.

Nonetheless, if one wishes to calculate  $P(\text{NS})$  using a non-parametric mass model, we provide a proof-of-concept below. Such a method could estimate classification probabilities  $P(\text{NS})$  directly from  $p(m|\Lambda)$ , bypassing the need for explicit parameters representing the NS-BH boundary.

We introduce a sample, two-stage edge detection procedure that scans the latent mass distribution for a sharp down turn consistent with the NS-BH boundary and report this as an estimate of the maximum non-rotating NS mass (which is then used to infer  $P(\text{NS})$ ). The algorithm operates on a mass grid  $m \in [1, 10]$  and requires a set of posterior draws from the population mass distribution  $p(m|\Lambda)$  (or any posterior distribution on a similar grid).

First, we apply a high frequency “inflection” filter, implemented as a second derivative (top hat) kernel, by convolving it with the mass function. This filter highlights abrupt curvature changes and edges. We selected the location of the peak filter response as our candidate  $m_{\max}^{\det}$ . If the resulting candidate lies in a physical realistic range  $2M_{\odot} < m_{\max}^{\det} < 5M_{\odot}$ , we accept it. Otherwise, we repeat the search with a broader “valley” filter, a local minimum kernel tuned to capture wide, gently sloping transitions. After convolving the second filter with the mass function, we once again select its peak filter response.

Since this method is purely filter based and works on  $p(m|\Lambda)$ , it is robust to specific parametric forms of the underlying population (i.e. this method works on any non-parametric mass model).

This is shown in the algorithm below. See [github.com/utkarsh7236/Guesswork-in-the-Gap](https://github.com/utkarsh7236/Guesswork-in-the-Gap) for the complete implementation.

---

**Algorithm 1:** Automatic detection of the NS–BH boundary

---

```

1: Input: Posterior mass probability  $p(m|\Lambda)$  on  $m \in [1, 10] M_{\odot}$ 
2: Compute log density:  $s(m) = \log_{10} p(m|\Lambda)$ 
3: Convolve  $s(m)$  with  $K_1$  (inflection kernel)  $\rightarrow r_1(m)$ 
4: Find candidate  $m^{\text{candidate}} = \arg \max |r_1(m)|$ 
5: if  $2.0 < m^{\text{candidate}} < 4.9$  then
6:   Accept  $m_{\max}^{\det} = m^{\text{candidate}}$ 
7: else
8:   Convolve  $s(m)$  with  $K_2$  (valley kernel)  $\rightarrow r_2(m)$ 
9:   Find  $m^{\text{candidate}} = \arg \max |r_2(m)|$ 
10:  Set  $m_{\max}^{\det} = m^{\text{candidate}}$ 
11: end if
12: Repeat steps 1–10 for all posterior draws to build the set  $\{m_{\max}^{\det}\}$ 
```

---

Referring to Figure 12, we find that the trends inferred from the parametric and non-parametric edge detection are remarkably similar across all hyperparameters considered. In both cases, the inferred  $P(\text{NS})$  remain consistent with one another. This consistency demonstrates the feasibility of such an analysis on weakly modeled mass distributions.

This method for detecting features is not particularly well explored. We have selected two detection schemes that, at best, may capture hints of structure in the mass distribution. They depend on a few heuristic criteria that are far from reliable. In principle, one could devise any number of similar algorithms to “discover” features marking the onset of the lower mass gap, each equally defensible. We restrict ourselves to two, as they perform adequately for illustrative purposes. Ultimately, these detection choices encode implicit priors and underscore the limitations of non-parametric approaches, which can often appear more objective than they actually are.

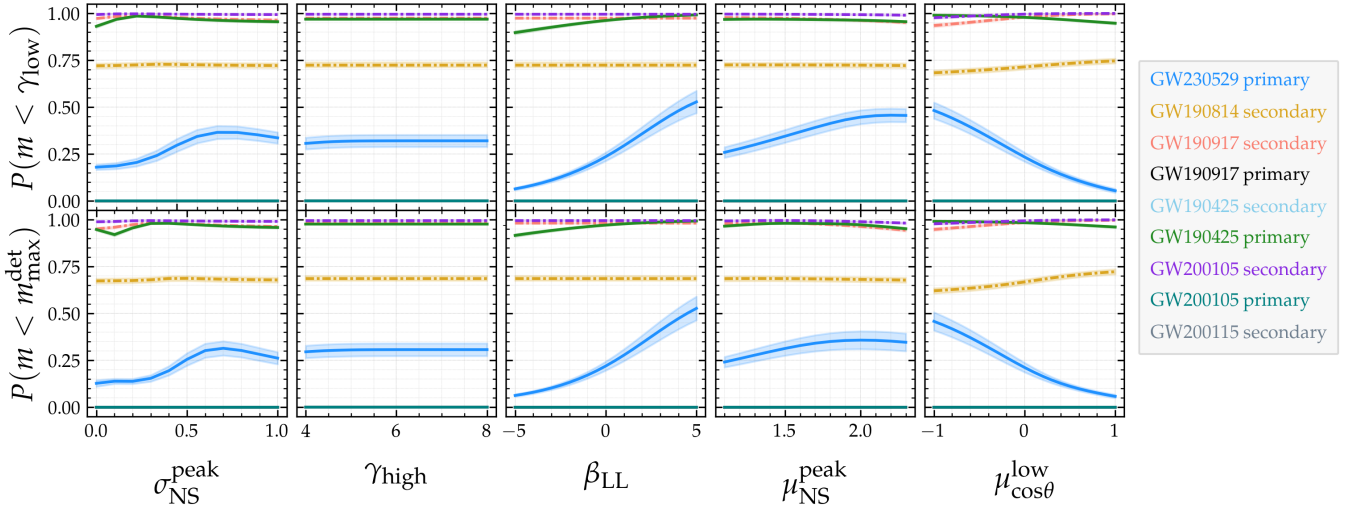


FIG. 12. **(Top)** Classification probabilities obtained with the parametric population model showing  $P(m < \gamma_{\text{low}})$ . **(Bottom)** the non-parametric method introduced in Appendix E  $P(m < m_{\text{max}}^{\text{det}})$ . Each panel varies one hyper-parameter. Across all parameters, the two approaches demonstrate remarkable agreement. Both identify the same similar changes in each event across the hyperparameter range. Overall, the consistency between methods validates our parametric results while demonstrating a proof-of-concept non-parametric approach (which can be applied to non-parametric mass models). The shaded region represents 90% credible interval around the mean. Primaries are solid lines and secondaries are dotted lines.

- [1] B. P. Abbott, R. Abbott, T. D. Abbott, and S. Abraham et al. GWTC-1: A Gravitational-Wave Transient Catalog of Compact Binary Mergers Observed by LIGO and Virgo during the First and Second Observing Runs. *Physical Review X*, 9(3):031040, September 2019. ISSN 2160-3308. doi:10.1103/PhysRevX.9.031040.
- [2] R. Abbott, T. D. Abbott, S. Abraham, F. Acernese, K. Ackley, A. Adams, and C. Adams et al. GWTC-2: Compact Binary Coalescences Observed by LIGO and Virgo During the First Half of the Third Observing Run. *Physical Review X*, 11(2):021053, June 2021. ISSN 2160-3308. doi:10.1103/PhysRevX.11.021053.
- [3] R. Abbott, T. D. Abbott, F. Acernese, K. Ackley, and C. Adams et al. GWTC-2.1: Deep extended catalog of compact binary coalescences observed by ligo and virgo during the first half of the third observing run. *Phys. Rev. D*, 109:022001, Jan 2024. doi: 10.1103/PhysRevD.109.022001.
- [4] R. Abbott, T. D. Abbott, F. Acernese, K. Ackley, and C. Adams et al. GWTC-3: Compact Binary Coalescences Observed by LIGO and Virgo During the Second Part of the Third Observing Run. *Physical Review X*, 13(4):041039, December 2023. ISSN 2160-3308. doi: 10.1103/PhysRevX.13.041039.
- [5] R. Abbott, T. D. Abbott, F. Acernese, K. Ackley, and C. Adams et al. The population of merging compact binaries inferred using gravitational waves through GWTC-3. *Physical Review X*, 13 (1):011048, March 2023. ISSN 2160-3308. doi: 10.1103/PhysRevX.13.011048.
- [6] A. G. Abac, I. Abouelfettouh, F. Acernese, K. Ackley, S. Adhicary, D. Adhikari, and N. Adhikari et al. GWTC-4.0: Methods for identifying and characterizing gravitational-wave transients, 2025. URL <https://arxiv.org/abs/2508.18081>.
- [7] A. G. Abac, I. Abouelfettouh, F. Acernese, K. Ackley, C. Adamcewicz, S. Adhicary, D. Adhikari, and N. Adhikari et al. GWTC-4.0: Updating the gravitational-wave transient catalog with observations from the first part of the Fourth LIGO-Virgo-KAGRA observing run, 2025. URL <https://arxiv.org/abs/2508.18082>.
- [8] F. Acernese, M. Agathos, K. Agatsuma, D. Aisa, N. Allemandou, A. Allocca, and J. Amarni et al. Advanced Virgo: a 2nd generation interferometric gravitational wave detector. *Classical and Quantum Gravity*, 32 (2):024001, January 2015. ISSN 0264-9381, 1361-6382. doi:10.1088/0264-9381/32/2/024001.
- [9] T Akutsu, M Ando, K Arai, Y Arai, and S Araki et al. Overview of KAGRA: Detector design and construction history. *Progress of Theoretical and Experimental Physics*, 2021(5):05A101, May 2021. ISSN 2050-3911. doi:10.1093/ptep/ptaa125.
- [10] J Aasi, B P Abbott, R Abbott, T Abbott, M R Abernathy, K Ackley, and C Adams et al. Advanced LIGO. *Classical and Quantum Gravity*, 32(7):074001, April 2015. ISSN 0264-9381, 1361-6382. doi:10.1088/0264-9381/32/7/074001.
- [11] B.P. Abbott, R. Abbott, T.D. Abbott, F. Acernese, K. Ackley, and C. Adams et al. GW170817: Observation of Gravitational Waves from a Binary Neutron Star Inspiral. *Physical Review Letters*, 119(16): 161101, October 2017. ISSN 0031-9007, 1079-7114. doi: 10.1103/PhysRevLett.119.161101.
- [12] B. P. Abbott, R. Abbott, T. D. Abbott, S. Abraham, F. Acernese, and K. Ackley et al. GW190425: Observation of a Compact Binary Coalescence with Total Mass  $3.4M_{\odot}$ . *The Astrophysical Journal Letters*, 892 (1):L3, March 2020. ISSN 2041-8205, 2041-8213. doi: 10.3847/2041-8213/ab75f5.
- [13] F. J. Fattoyev, C. J. Horowitz, J. Piekarewicz, and Brendan Reed. GW190814: Impact of a 2.6 solar mass neutron star on nucleonic equations of state. *Physical Review C*, 102(6):065805, December 2020. ISSN 2469-9985, 2469-9993. doi:10.1103/PhysRevC.102.065805.
- [14] Daniel A. Godzieba, David Radice, and Sebastiano Bernuzzi. On the maximum mass of neutron stars and GW190814. *The Astrophysical Journal*, 908(2): 122, February 2021. ISSN 0004-637X, 1538-4357. doi: 10.3847/1538-4357/abd4dd.
- [15] Elias R. Most, L. Jens Papenfort, Lukas R. Weih, and Luciano Rezzolla. A lower bound on the maximum mass if the secondary in GW190814 was once a rapidly spinning neutron star. *Monthly Notices of the Royal Astronomical Society: Letters*, 499(1):L82–L86, October 2020. ISSN 1745-3925, 1745-3933. doi: 10.1093/mnrasl/slaa168.
- [16] R. Abbott, T. D. Abbott, S. Abraham, F. Acernese, K. Ackley, A. Adams, and C. Adams et al. Observation of gravitational waves from two neutron star-black hole coalescences. *The Astrophysical Journal Letters*, 915 (1):L5, July 2021. ISSN 2041-8205, 2041-8213. doi: 10.3847/2041-8213/ac082e.
- [17] A. G. Abac, R. Abbott, I. Abouelfettouh, F. Acernese, K. Ackley, S. Adhicary, and N. Adhikari et al. Observation of Gravitational Waves from the Coalescence of a  $2.5 - 4.5M_{\odot}$  Compact Object and a Neutron Star. *The Astrophysical Journal Letters*, 970(2):L34, jul 2024. doi: 10.3847/2041-8213/ad5beb.
- [18] Eemeli Annala, Tyler Gorda, Aleksi Kurkela, Joonas Nättälä, and Aleksi Vuorinen. Evidence for quark-matter cores in massive neutron stars. *Nature Physics*, 16(9):907–910, September 2020. ISSN 1745-2481. doi: 10.1038/s41567-020-0914-9.
- [19] John Antoniadis, Paulo C. C. Freire, Norbert Wex, and Tauriset al. A Massive Pulsar in a Compact Relativistic Binary. *Science*, 340(6131):1233232, April 2013. doi: 10.1126/science.1233232.
- [20] Paul Demorest, Tim Pennucci, Scott Ransom, Mallory Roberts, and Jason Hessels. Shapiro delay measurement of a two solar mass neutron star. *Nature*, 467(7319): 1081–1083, October 2010. ISSN 0028-0836, 1476-4687. doi:10.1038/nature09466.
- [21] E. Fonseca, H. T. Cromartie, T. T. Pennucci, and P. S. Ray et al. Refined Mass and Geometric Measurements of the High-mass PSR J0740+6620. *The Astrophysical Journal*, 915:L12, July 2021. ISSN 0004-637X. doi: 10.3847/2041-8213/ac03b8.
- [22] S. Gandolfi, J. Carlson, and Sanjay Reddy. Maximum mass and radius of neutron stars, and the nuclear symmetry energy. *Physical Review C*, 85(3):032801, March 2012. doi:10.1103/PhysRevC.85.032801.
- [23] Vassiliki Kalogera and Gordon Baym. The Maximum

- Mass of a Neutron Star. *The Astrophysical Journal*, 470(1):L61–L64, October 1996. ISSN 0004-637X. doi: 10.1086/310296.
- [24] Isaac Legred, Katerina Chatzioannou, Reed Essick, Sophia Han, and Philippe Landry. Impact of the PSR J0740+6620 radius constraint on the properties of high-density matter. *Physical Review D*, 104(6):063003, September 2021. doi:10.1103/PhysRevD.104.063003.
- [25] M. Linares, T. Shahbaz, and J. Casares. Peering into the Dark Side: Magnesium Lines Establish a Massive Neutron Star in PSR J2215+5135. *The Astrophysical Journal*, 859:54, May 2018. ISSN 0004-637X. doi: 10.3847/1538-4357/aabde6.
- [26] Ben Margalit and Brian Metzger. Constraining the Maximum Mass of Neutron Stars From Multi-Messenger Observations of GW170817. *The Astrophysical Journal Letters*, 850(2):L19, December 2017. ISSN 2041-8205, 2041-8213. doi:10.3847/2041-8213/aa991c.
- [27] M. C. Miller, F. K. Lamb, A. J. Dittmann, S. Bogdanov, and Z. et al. Arzoumanian. The Radius of PSR J0740+6620 from NICER and XMM-Newton Data. *The Astrophysical Journal Letters*, 918(2):L28, September 2021. ISSN 2041-8205, 2041-8213. doi:10.3847/2041-8213/ac089b.
- [28] J. R. Oppenheimer and G. M. Volkoff. On Massive Neutron Cores. *Physical Review*, 55(4):374–381, February 1939. doi:10.1103/PhysRev.55.374.
- [29] Feryal Özel and Paulo Freire. Masses, Radii, and the Equation of State of Neutron Stars. *Annual Review of Astronomy and Astrophysics*, 54(Volume 54, 2016):401–440, September 2016. ISSN 0066-4146, 1545-4282. doi: 10.1146/annurev-astro-081915-023322.
- [30] M. Prakash, T. L. Ainsworth, and J. M. Lattimer. Equation of State and the Maximum Mass of Neutron Stars. *Physical Review Letters*, 61(22):2518–2521, November 1988. doi:10.1103/PhysRevLett.61.2518.
- [31] Luciano Rezzolla, Elias R. Most, and Lukas R. Weih. Using gravitational-wave observations and quasi-universal relations to constrain the maximum mass of neutron stars. *The Astrophysical Journal Letters*, 852(2):L25, January 2018. ISSN 2041-8205, 2041-8213. doi: 10.3847/2041-8213/aaa401.
- [32] Clifford E. Rhoades and Remo Ruffini. Maximum Mass of a Neutron Star. *Physical Review Letters*, 32(6):324–327, February 1974. doi:10.1103/PhysRevLett.32.324.
- [33] Roger W. Romani, D. Kandel, Alexei V. Filippenko, Thomas G. Brink, and WeiKang Zheng. PSR J0952-0607: The Fastest and Heaviest Known Galactic Neutron Star. *The Astrophysical Journal Letters*, 934(2):L17, August 2022. ISSN 2041-8205, 2041-8213. doi: 10.3847/2041-8213/ac8007.
- [34] Masaru Shibata, Enping Zhou, Kenta Kiuchi, and Sho Fujibayashi. Constraint on the maximum mass of neutron stars using GW170817 event. *Physical Review D*, 100(2):023015, July 2019. ISSN 2470-0010, 2470-0029. doi:10.1103/PhysRevD.100.023015.
- [35] Richard C. Tolman. Static Solutions of Einstein’s Field Equations for Spheres of Fluid. *Physical Review*, 55(4): 364–373, February 1939. doi:10.1103/PhysRev.55.364.
- [36] Krzysztof Belczynski, Tomasz Bulik, Ilya Mandel, B. S. Sathyaprakash, Andrzej Zdziarski, and Joanna Mikolajewska. Cyg X-3: a Galactic double black hole or black hole-neutron star progenitor. *The Astrophysical Journal*, 764(1):96, January 2013. ISSN 0004-637X, 1538-4357. doi:10.1088/0004-637X/764/1/96.
- [37] Chirag Chawla, Sourav Chatterjee, Katelyn Breivik, Chaithanya Krishna Moorthy, Jeff J. Andrews, and Robyn E. Sanderson. Gaia May Detect Hundreds of Well-characterized Stellar Black Holes. *The Astrophysical Journal*, 931(2):107, May 2022. ISSN 0004-637X. doi:10.3847/1538-4357/ac60a5.
- [38] R. Abbott, T. D. Abbott, F. Acernese, K. Ackley, and C. Adams et al. The population of merging compact binaries inferred using gravitational waves through GWTC-3. *Physical Review X*, 13(1):011048, March 2023. ISSN 2160-3308. doi: 10.1103/PhysRevX.13.011048.
- [39] Will M. Farr, Niharika Sravan, Andrew Cantrell, Laura Kreidberg, Charles D. Bailyn, Ilya Mandel, and Vicky Kalogera. The Mass Distribution of Stellar-mass Black Holes. *The Astrophysical Journal*, 741:103, November 2011. ISSN 0004-637X. doi:10.1088/0004-637X/741/2/103.
- [40] Maya Fishbach, Reed Essick, and Daniel E. Holz. Does Matter Matter? Using the Mass Distribution to Distinguish Neutron Stars and Black Holes. *The Astrophysical Journal Letters*, 899(1):L8, August 2020. ISSN 2041-8205. doi:10.3847/2041-8213/aba7b6.
- [41] T. Jayasinghe, K. Z. Stanek, Todd A. Thompson, C. S. Kochanek, and D. M. et al. Rowan. A Unicorn in Monoceros: the  $3M_{\odot}$  dark companion to the bright, nearby red giant V723 Mon is a non-interacting, mass-gap black hole candidate. *Monthly Notices of the Royal Astronomical Society*, 504(2):2577–2602, May 2021. ISSN 0035-8711, 1365-2966. doi:10.1093/mnras/stab907.
- [42] Tyson B. Littenberg, Benjamin Farr, Scott Coughlin, Vicky Kalogera, and Daniel E. Holz. Neutron stars versus black holes: probing the mass gap with LIGO/Virgo. *The Astrophysical Journal*, 807(2):L24, July 2015. ISSN 2041-8213. doi:10.1088/2041-8205/807/2/L24.
- [43] Todd A. Thompson, Christopher S. Kochanek, Krzysztof Z. Stanek, and Carles et al. Badenes. Discovery of a Candidate Black Hole - Giant Star Binary System in the Galactic Field. *Science*, 366(6465):637–640, November 2019. ISSN 0036-8075, 1095-9203. doi: 10.1126/science.aau4005.
- [44] S. E. Woosley. The Evolution of Massive Helium Stars Including Mass Loss. *The Astrophysical Journal*, 878(1):49, June 2019. ISSN 0004-637X, 1538-4357. doi: 10.3847/1538-4357/ab1b41.
- [45] Christine Ye and Maya Fishbach. Inferring the Neutron Star Maximum Mass and Lower Mass Gap in Neutron Star–Black Hole Systems with Spin. *The Astrophysical Journal*, 937(2):73, September 2022. ISSN 0004-637X. doi:10.3847/1538-4357/ac7f99.
- [46] Claire S. Ye, Kyle Kremer, Scott M. Ransom, and Frederic A. Rasio. Lower-mass-gap Black Holes in Dense Star Clusters. *The Astrophysical Journal*, 975(1):77, November 2024. ISSN 0004-637X, 1538-4357. doi: 10.3847/1538-4357/ad76a0.
- [47] Zepei Xing, Vicky Kalogera, Tassos Fragos, Jeff J. Andrews, Simone S. Bavera, Max Briel, Seth Gossege, Konstantinos Kovlakas, Matthias U. Kruckow, Kyle Akira Rocha, Meng Sun, Philipp M. Srivastava, and Emmanuel Zapartas. Mass-gap Black Holes in Coalescing Neutron Star–Black Hole Binaries. *The Astro-*

- physical Journal*, 989(2):188, August 2025. ISSN 0004-637X. doi:10.3847/1538-4357/adec6d.
- [48] Chris L. Fryer, Krzysztof Belczynski, Grzegorz Wiktorowicz, Michal Dominik, Vicky Kalogera, and Daniel E. Holz. Compact Remnant Mass Function: Dependence on the explosion mechanism and metallicity. *The Astrophysical Journal*, 749(1):91, March 2012. ISSN 0004-637X. doi:10.1088/0004-637X/749/1/91.
- [49] Laura Kreidberg, Charles D. Bailyn, Will M. Farr, and Vassiliki Kalogera. Mass Measurements of Black Holes in X-Ray Transients: Is There a Mass Gap? *The Astrophysical Journal*, 757(1):36, September 2012. ISSN 0004-637X, 1538-4357. doi:10.1088/0004-637X/757/1/36.
- [50] Will M. Farr, Niharika Sravan, Andrew Cantrell, Laura Kreidberg, Charles D. Bailyn, Ilya Mandel, and Vicky Kalogera. The Mass Distribution of Stellar-Mass Black Holes. *The Astrophysical Journal*, 741(2):103, November 2011. ISSN 0004-637X, 1538-4357. doi:10.1088/0004-637X/741/2/103.
- [51] Krzysztof Belczynski, Grzegorz Wiktorowicz, Chris L. Fryer, Daniel E. Holz, and Vassiliki Kalogera. Missing black holes unveil the supernova explosion mechanism. *The Astrophysical Journal*, 757(1):91, September 2012. ISSN 0004-637X. doi:10.1088/0004-637X/757/1/91.
- [52] Chris L. Fryer, Aleksandra Olejak, and Krzysztof Belczynski. The Effect of Supernova Convection On Neutron Star and Black Hole Masses. *The Astrophysical Journal*, 931(2):94, May 2022. ISSN 0004-637X. doi:10.3847/1538-4357/ac6ac9.
- [53] C. S. Kochanek. Failed supernovae explain the compact remnant mass function. *The Astrophysical Journal*, 785(1):28, March 2014. ISSN 0004-637X. doi:10.1088/0004-637X/785/1/28.
- [54] Tong Liu, Yun-Feng Wei, Li Xue, and Mou-Yuan Sun. Final Compact Remnants in Core-collapse Supernovae from 20 to 40  $M_{\odot}$ : The Lower Mass Gap. *The Astrophysical Journal*, 908(1):106, February 2021. ISSN 0004-637X. doi:10.3847/1538-4357/abd24e.
- [55] Shi-Jie Gao, Xiang-Dong Li, and Yong Shao. Formation of mass-gap black holes from neutron star X-ray binaries with super-Eddington accretion. *Monthly Notices of the Royal Astronomical Society*, 514(1):1054–1070, July 2022. ISSN 0035-8711. doi:10.1093/mnras/stac1426.
- [56] Jared C. Siegel, Ilia Kiato, and Vicky et al. Kalogera. Investigating the Lower Mass Gap with Low-mass X-Ray Binary Population Synthesis. *The Astrophysical Journal*, 954(2):212, September 2023. ISSN 0004-637X. doi:10.3847/1538-4357/ace9d9.
- [57] John Antoniadis, Paulo C. C. Freire, Norbert Wex, Thomas M. Tauris, and Ryan S. et al. Lynch. A Massive Pulsar in a Compact Relativistic Binary. *Science*, 340:448, April 2013. ISSN 0036-8075. doi:10.1126/science.1233232.
- [58] K. Belczynski, G. Wiktorowicz, C. Fryer, D. Holz, and V. Kalogera. Missing Black Holes Unveil The Supernova Explosion Mechanism. *The Astrophysical Journal*, 757(1):91, September 2012. ISSN 0004-637X, 1538-4357. doi:10.1088/0004-637X/757/1/91.
- [59] R. Abbott, T. D. Abbott, S. Abraham, and F. Acernece et al. GW190814: Gravitational Waves from the Coalescence of a  $23 M_{\odot}$  Black Hole with a  $2.6 M_{\odot}$  Compact Object. *The Astrophysical Journal Letters*, 896(2):L44, June 2020. ISSN 2041-8205, 2041-8213. doi:10.3847/2041-8213/ab960f.
- [60] P. B. Demorest, T. Pennucci, S. M. Ransom, M. S. E. Roberts, and J. W. T. Hessels. A two-solar-mass neutron star measured using Shapiro delay. *Nature*, 467(7319):1081–1083, October 2010. ISSN 1476-4687. doi:10.1038/nature09466.
- [61] Amanda M. Farah, Maya Fishbach, Reed Essick, Daniel E. Holz, and Shanika Galauadage. Bridging the Gap: Categorizing Gravitational-Wave Events at the Transition Between Neutron Stars and Black Holes. *The Astrophysical Journal*, 931(2):108, June 2022. ISSN 0004-637X, 1538-4357. doi:10.3847/1538-4357/ac5f03.
- [62] E. Fonseca, H. T. Cromartie, T. T. Pennucci, and P. S. Ray et al. Refined Mass and Geometric Measurements of the High-mass PSR J0740+6620. *The Astrophysical Journal*, 915:L12, July 2021. ISSN 0004-637X. doi:10.3847/2041-8213/ac03b8.
- [63] C. L. Fryer, K. Belczynski, G. Wiktorowicz, M. Dominik, V. Kalogera, and D. Holz. Compact Remnant Mass Function: Dependence on the Explosion Mechanism and Metallicity. *The Astrophysical Journal*, 749(1):91, April 2012. ISSN 0004-637X, 1538-4357. doi:10.1088/0004-637X/749/1/91.
- [64] Todd A. Thompson, Christopher S. Kochanek, Krzysztof Z. Stanek, Carles Badenes, and et al. Post. A noninteracting low-mass black hole–giant star binary system. *Science*, 366(6465):637–640, November 2019. doi:10.1126/science.aau4005.
- [65] Christine Ye and Maya Fishbach. Inferring the neutron star maximum mass and lower mass gap in neutron star-black hole systems with spin. *The Astrophysical Journal*, 937(2):73, October 2022. ISSN 0004-637X, 1538-4357. doi:10.3847/1538-4357/ac7f99.
- [66] Ivan Markin, Anna Puecher, Mattia Bulla, and Tim Dietrich. Challenging a binary neutron star merger interpretation of GW230529, 2025. URL <https://arxiv.org/abs/2508.08750>.
- [67] Jessica Cotturone, Michael Zevin, and Sylvia Biscoveanu. Characterizing compact object binaries in the lower mass gap with gravitational waves, 2025. URL <https://arxiv.org/abs/2507.01189>.
- [68] A. Akmal, V. R. Pandharipande, and D. G. Ravenhall. Equation of state of nucleon matter and neutron star structure. *Physical Review C*, 58(3):1804–1828, September 1998. doi:10.1103/PhysRevC.58.1804.
- [69] F. Douchin and P. Haensel. A unified equation of state of dense matter and neutron star structure. *Astronomy & Astrophysics*, 380(1):151–167, December 2001. ISSN 0004-6361, 1432-0746. doi:10.1051/0004-6361:20011402.
- [70] Eliot Finch, Isaac Legred, Katerina Chatzioannou, Reed Essick, Sophia Han, and Philippe Landry. Unified nonparametric equation-of-state inference from the neutron-star crust to perturbative-qcd densities. *Physical Review D*, 112(10), November 2025. ISSN 2470-0029. doi:10.1103/krc7-kz2l.
- [71] B. Friedman and V. R. Pandharipande. Hot and cold, nuclear and neutron matter. *Nuclear Physics A*, 361(2):502–520, May 1981. ISSN 0375-9474. doi:10.1016/0375-9474(81)90649-7.
- [72] Jacob Golomb, Isaac Legred, Katerina Chatzioannou, and Philippe Landry. Interplay of astrophysics and nuclear physics in determining the properties of neutron stars. *Physical Review D*, 111(2), January 2025. ISSN 2470-0029. doi:10.1103/physrevd.111.023029.

- [73] G. A. Lalazissis, J. König, and P. Ring. New parametrization for the Lagrangian density of relativistic mean field theory. *Physical Review C*, 55(1):540–543, January 1997. doi:10.1103/PhysRevC.55.540.
- [74] Philippe Landry, Reed Essick, and Katerina Chatzioannou. Nonparametric constraints on neutron star matter with existing and upcoming gravitational wave and pulsar observations. *Physical Review D*, 101(12):123007, June 2020. ISSN 2470-0010, 2470-0029. doi:10.1103/PhysRevD.101.123007.
- [75] Sailesh Ranjan Mohanty, Utkarsh Mali, H. C. Das, Bharat Kumar, and Philippe Landry. Astrophysical constraints on neutron star  $f$ -modes with a nonparametric equation of state representation, 2024. URL <https://arxiv.org/abs/2410.16689>.
- [76] Sunny Ng, Isaac Legred, Lami Suleiman, Philippe Landry, Lyla Traylor, and Jocelyn Read. Inferring the neutron star equation of state with nuclear-physics informed semiparametric models. *Classical and Quantum Gravity*, 42(20):205008, October 2025. ISSN 1361-6382. doi:10.1088/1361-6382/ae1094.
- [77] R. B. Wiringa, V. Fiks, and A. Fabrocini. Equation of state for dense nucleon matter. *Physical Review C*, 38(2):1010–1037, August 1988. doi:10.1103/PhysRevC.38.1010.
- [78] A. Bauswein, T. W. Baumgarte, and H.-T. Janka. Prompt merger collapse and the maximum mass of neutron stars. *Physical Review Letters*, 111(13), September 2013. ISSN 1079-7114. doi:10.1103/physrevlett.111.131101.
- [79] Cosima Breu and Luciano Rezzolla. Maximum mass, moment of inertia and compactness of relativistic stars. *Monthly Notices of the Royal Astronomical Society*, 459(1):646–656, June 2016. ISSN 0035-8711, 1365-2966. doi:10.1093/mnras/stw575.
- [80] Utkarsh Mali and Reed Essick. Striking a Chord with Spectral Sirens: Multiple features in the compact binary population correlate with  $h_0$ . *The Astrophysical Journal*, 980(1):85, feb 2025. doi:10.3847/1538-4357/ad9de7. URL <https://doi.org/10.3847/1538-4357/ad9de7>.
- [81] A. G. Abac, I. Abouelfettouh, F. Acernese, K. Ackley, C. Adamcewicz, S. Adhikary, D. Adhikari, and N. Adhikari et al. GWTC-4.0: Population properties of merging compact binaries, 2025. URL <https://arxiv.org/abs/2508.18083>.
- [82] Reed Essick and Philippe Landry. Discriminating between Neutron Stars and Black Holes with Imperfect Knowledge of the Maximum Neutron Star Mass. *The Astrophysical Journal*, 904(1):80, November 2020. doi:10.3847/1538-4357/abbd3b.
- [83] Reed Essick and Maya Fishbach. Ensuring Consistency between Noise and Detection in Hierarchical Bayesian Inference. *The Astrophysical Journal*, 962(2):169, feb 2024. doi:10.3847/1538-4357/ad1604. URL <https://doi.org/10.3847/1538-4357/ad1604>.
- [84] Reed Essick. Semianalytic sensitivity estimates for catalogs of gravitational-wave transients. *Phys. Rev. D*, 108:043011, Aug 2023. doi:10.1103/PhysRevD.108.043011.
- [85] Reed Essick, Michael W. Coughlin, Michael Zevin, Deep Chatterjee, Teagan A. Clarke, Storm Colloms, Utkarsh Mali, and Simona Miller et al. Compact binary coalescence sensitivity estimates with injection campaigns during the LIGO-Virgo-KAGRA Collaborations’ fourth observing run. *Phys. Rev. D*, 112:102001, Nov 2025. doi:10.1103/44x3-hv3y. URL <https://link.aps.org/doi/10.1103/44x3-hv3y>.
- [86] T. A. Callister. Observed gravitational-wave populations, 2024. URL <https://arxiv.org/abs/2410.19145>.
- [87] Ilya Mandel, Will M. Farr, and Jonathan R. Gair. Extracting distribution parameters from multiple uncertain observations with selection biases. *Monthly Notices of the Royal Astronomical Society*, 486(1):1086–1093, June 2019. ISSN 0035-8711, 1365-2966. doi:10.1093/mnras/stz896.
- [88] Ilya Mandel. Parameter estimation on gravitational waves from multiple coalescing binaries. *Physical Review D*, 81(8):084029, April 2010. ISSN 1550-7998, 1550-2368. doi:10.1103/PhysRevD.81.084029.
- [89] John Skilling. Nested Sampling. In *Bayesian Inference and Maximum Entropy Methods in Science and Engineering: 24th International Workshop on Bayesian Inference and Maximum Entropy Methods in Science and Engineering*, volume 735, pages 395–405, November 2004. doi:10.1063/1.1835238.
- [90] Eric Thrane and Colm Talbot. An introduction to Bayesian inference in gravitational-wave astronomy: parameter estimation, model selection, and hierarchical models. *Publications of the Astronomical Society of Australia*, 36:e010, 2019. ISSN 1323-3580, 1448-6083. doi:10.1017/pasa.2019.2.
- [91] M. Drago, V. Gayathri, S. Klimenko, and C. et al. Lazzaro. Coherent WaveBurst, a pipeline for unmodeled gravitational-wave data analysis. *SoftwareX*, 14:100678, June 2021. ISSN 23527110. doi:10.1016/j.softx.2021.100678.
- [92] Kipp Cannon, Sarah Caudill, Chiwai Chan, Bryce Cousins, Jolien D. E. Creighton, Becca Ewing, Heather Fong, Patrick Godwin, Chad Hanna, Shaun Hooper, Rachael Huxford, Ryan Magee, Duncan Meacher, Cody Messick, Soichiro Morisaki, Debnandini Mukherjee, Hiroaki Ohta, Alexander Pace, Stephen Privitera, Iris de Ruiter, Surabhi Sachdev, Leo Singer, Divya Singh, Ron Tapia, Leo Tsukada, Daichi Tsuna, Takuya Tsutsui, Koh Ueno, Aaron Viets, Leslie Wade, and Madeline Wade. Gstlal: A software framework for gravitational wave discovery, 2020. URL <https://arxiv.org/abs/2010.05082>.
- [93] Florian Aubin, Francesco Brighenti, Roberto Chierici, Dimitri Estevez, Giuseppe Greco, Gianluca Maria Guidi, Vincent Juste, Frédérique Marion, Benoit Mouris, Elisa Nitoglia, Orion Sauter, and Viola Sordini. The MBTA Pipeline for Detecting Compact Binary Coalescences in the Third LIGO-Virgo Observing Run. *Classical and Quantum Gravity*, 38(9):095004, May 2021. ISSN 0264-9381, 1361-6382. doi:10.1088/1361-6382/abe913.
- [94] Samantha A. Usman, Alexander H. Nitz, Ian W. Harry, Christopher M. Biwer, Duncan A. Brown, Miriam Cabero, Collin D. Capano, Tito Dal Canton, Thomas Dent, Stephen Fairhurst, Marcel S. Kehl, Drew Keppel, Badri Krishnan, Amber Lenon, Andrew Lundgren, Alex B. Nielsen, Larne P. Pekowsky, Harald P. Pfeiffer, Peter R. Saulson, Matthew West, and Joshua L. Willis. The PyCBC search for gravitational waves from compact binary coalescence. *Classical and Quantum Gravity*, 33(21):215004, November 2016. ISSN 0264-9381, 1361-6382. doi:10.1088/0264-9381/33/21/215004.

- [95] LIGO Scientific Collaboration, Virgo Collaboration, and KAGRA Collaboration. GWTC-3: Compact binary coalescences observed by LIGO and virgo during the second part of the third observing run — O1+O2+O3 search sensitivity estimates, November 2021.
- [96] R. Abbott, T. D. Abbott, F. Acernese, K. Ackley, and C. Adams et al. The population of merging compact binaries inferred using gravitational waves through GWTC-3. *Physical Review X*, 13(1):011048, March 2023. ISSN 2160-3308. doi: 10.1103/PhysRevX.13.011048.
- [97] L. A. C. van Son, S. K. Roy, I. Mandel, W. M. Farr, A. Lam, J. Merritt, F. S. Broekgaarden, A. A. C. Sander, and J. J. Andrews. Not just winds: Why models find that binary black hole formation is metallicity-dependent, while binary neutron star formation is not. *The Astrophysical Journal*, 979(2):209, jan 2025. doi: 10.3847/1538-4357/ada14a.
- [98] Reed Essick. `mmax-model-selection`. <https://git.ligo.org/reed.essick/mmax-model-selection>, 2023.
- [99] Reed Essick et al. `gw-distributions`. <https://git.ligo.org/reed.essick/gw-distributions>, 2023.
- [100] Note1. In theory,  $H$  can be any background information.
- [101] Ryan J. Foley, David A. Coulter, Charles D. Kilpatrick, Anthony L. Piro, Enrico Ramirez-Ruiz, and Josiah Schwab. Updated Parameter Estimates for GW190425 Using Astrophysical Arguments and Implications for the Electromagnetic Counterpart. *Monthly Notices of the Royal Astronomical Society*, 494(1):190–198, May 2020. ISSN 0035-8711, 1365-2966. doi: 10.1093/mnras/staa725.
- [102] Bulent Kiziltan, Athanasios Kottas, Maria De Yoreo, and Stephen E. Thorsett. The Neutron Star Mass Distribution. *The Astrophysical Journal*, 778(1):66, November 2013. ISSN 0004-637X, 1538-4357. doi: 10.1088/0004-637X/778/1/66.
- [103] Planck Collaboration, P. A. R. Ade, N. Aghanim, M. Arnaud, M. Ashdown, J. Aumont, C. Baccigalupi, A. J. Banday, R. B. Barreiro, J. G. Bartlett, N. Bartolo, and et al. Battaner. Planck 2015 results. XIII. Cosmological parameters. *Astronomy & Astrophysics*, 594: A13, October 2016. ISSN 0004-6361, 1432-0746. doi: 10.1051/0004-6361/201525830.